

Gravitational Waves From More Attractive Dark Binaries

Yang Bai^a, Sida Lu^b, and Nicholas Orlofsky^c

^a*Department of Physics, University of Wisconsin-Madison, Madison, WI 53706, USA*

^b*Institute for Advanced Study, The Hong Kong University of Science and Technology, Clear Water Bay, Kowloon, Hong Kong S.A.R., P. R. China*

^c*Institute of Theoretical Physics, Faculty of Physics, University of Warsaw, ul. Pasteura 5, PL-02-093 Warsaw, Poland*

Abstract

The detection of gravitational waves (GWs) has led to a deeper understanding of binaries of ordinary astrophysical objects, including neutron stars and black holes. In this work, we point out that binary systems may also exist in a dark sector with astrophysical-mass macroscopic dark matter. These “dark binaries,” when coupled to an additional attractive long-range dark force, may generate a stochastic gravitational wave background (SGWB) with a characteristic spectrum different from ordinary binaries. We find that the SGWB from planet-mass dark binaries is detectable by space- and ground-based GW observatories. The contribution to the SGWB today is smaller from binaries that merge before recombination than after, avoiding constraints on extra radiation degrees of freedom while potentially leaving a detectable GW signal at high frequencies up to tens of GHz.

Contents

1	Introduction	2
2	Macroscopic dark matter with a dark long-range force	3
3	Dark force mediation and radiation	7
4	Merger Rate and Stochastic GW Spectrum	10
5	Properties of and constraints on the SGWB	14
5.1	An analytic understanding of the SGWB spectrum	14
5.2	Experimental sensitivity	16
5.2.1	Ground- and satellite-based interferometers	16
5.2.2	High frequency GW signals	19
6	Discussion and conclusions	22
A	Dark quark nugget effective charge for the scalar-mediator model	24
B	Radiation emission from a binary with a massless dark force mediator	25
B.1	GW emission	25
B.2	Dark force mediator emission	26
B.2.1	Vector mediator	26
B.2.2	Scalar mediator	27
C	More details on the shape of the GW spectra	30
D	GW emission at higher harmonics	34

1 Introduction

The recent evidence of a stochastic gravitational wave background (SGWB) using pulsar timing arrays (PTAs) from NANOGrav [1–4], EPTA and InPTA [5–8], PPTA [9–11], and CPTA [12] following the first direct detection of gravitational waves (GWs) [13] at LIGO [14] offers an entirely new way to measure the properties and contents of the Universe. GWs have already provided a window into the mergers of both stellar-mass black holes (BHs) and neutron stars [15–17], and the SGWB also gives insight into supermassive BHs [4, 8]. With other observatories like LISA [18] and SKA [19] in development, as well as several proposed observatories under active consideration [20–25], the mystery of GWs over a larger frequency band will soon be unveiled with good precision.

Besides employing GWs for understanding astrophysical objects, one can also harness GWs, especially the SGWB, to investigate early-universe physics within or beyond the Standard Model (BSM). Due to the graviton’s ultra-weak interactions with other particles in the early universe, GWs serve as an excellent “cosmic envoy,” potentially containing information about the Universe’s history as early as the inflation era. For example, first-order phase transitions at the QCD and/or electroweak scales might produce SGWBs of sufficient magnitude to be observable with the LISA telescope (see Ref. [26] for a recent review and Refs. [3, 8, 27] for more general discussion in light of the first SGWB signal). Unlike SGWB sources generated in nonequilibrium environments, this work focuses on a novel source of SGWB from BSM: “dark binaries” or binaries comprised of two macroscopic dark matter (MDM) objects.

The SGWB signal from the mergers of MDM objects such as primordial BHs has been a topic of recent interest [28–36]. A majority of MDM binaries are expected to form in the early universe, before matter-radiation equality [30, 37–43]. These binaries then inspiral and merge throughout cosmic time, and the GWs they emit contribute to the SGWB. The SGWB signal is fundamentally limited by the fact that gravity controls all the dynamics of the binary system, determining its orbital parameters and emission of energy. Thus, for example, very light MDM will not produce a detectable signal because the amplitude of the emitted GW spectrum is directly related to the mass.

However, MDM need not only couple to gravity. In general, the dark sector may contain a variety of fields and forces, much like the visible sector. If a long-range dark force (DF) exists that couples solely to dark sector states, it can modify the SGWB signal in a number of ways. For concreteness, consider an attractive DF. First, the orbital dynamics are modified. With an attractive DF, the orbital frequency increases, leading to GW emission with both higher amplitude and frequency. Second, the binary binding energy is altered, allowing more energy to be released as radiation. Third, the MDM binary can emit the DF mediator as radiation in addition to GWs. While this does remove some energy that could be emitted as GWs, it also shortens the binary merger time (for fixed initial orbital parameters), which can enhance the merger rate. Fourth and finally, a pair of MDM objects can more easily find each other in the early universe, allowing them to form earlier and with smaller initial separation. This tends to enhance the merger rate and, consequently, the SGWB. However, in more extreme cases, the binaries may merge too early, resulting in the redshifting away of their GWs.

This work evaluates all of these effects. In particular, we demonstrate that the inclusion of the DF can enhance the SGWB from MDM binaries, rendering it more detectable for GW

observatories across the frequency spectrum—from nHz at PTAs up through kHz at terrestrial interferometers like LIGO. DF-mediated MDM binaries may even present a novel target for high-frequency GW detectors. The binary-sourced SGWB can be sufficiently small during recombination to evade constraints on additional dark radiation degrees of freedom, but later grow larger as more binaries merge, potentially becoming detectable. Related work exploring the inclusion of additional forces for binaries in the visible rather than dark sector can be found in Refs. [44–46].

Note that MDMs may make up either some or all of dark matter (DM). For masses above 10^{23} g up to order solar mass, they are generally constrained by microlensing to be less than about 10^{-1} to 10^{-2} of DM, depending on their mass and radius [47–57]. Future searches may extend to smaller (currently unconstrained) masses [58–60]. For masses above solar mass, their abundance is even more strongly constrained by accretion [57, 61–64], star survival in dwarf galaxies [65, 66], and Lyman- α [67, 68]. Constraints on a long-range DF also exist, but they are generally fairly weak if the range is less than of order tens of kiloparsecs [69, 70]. This work assumes that the DF mediator is approximately massless in comparison to all other scales in the problem while remaining compliant with existing bounds, with the case of a more massive mediator briefly discussed in the last section but ultimately left for future work.

This work is organized as follows. Sec. 2 discusses models for MDM with a long-range DF. Readers who are less interested in models and more interested in phenomenology may skip to Sec. 3, which introduces a model-independent treatment of the radiation of both GWs and DF mediators from binaries in the presence of the new DF. Sec. 4 discusses the calculation of the binary formation and subsequent merger rate, and then combines this with the results of the Sec. 3 to calculate the SGWB spectrum. Sec. 5 analyzes the SGWB spectrum both analytically and numerically and compares against existing and future GW observatory sensitivities. Finally, discussion and conclusions are presented in Sec. 6.

2 Macroscopic dark matter with a dark long-range force

Independent of the ultralight DF mediator, MDM is assumed to form at an early time in the cosmological history. Among many macroscopic dark matter models, we choose the “dark quark nugget” (DQN) [71] as a representative (see also [72–74]). In this class of models, the DQNs are made of dark quarks that are in the deconfined phase of the underlying dark quantum chromodynamics (dQCD), with the Lagrangian as

$$\mathcal{L}_{\text{dQCD}} = \sum_{i=1}^{N_f} [\bar{\psi}_i i\gamma^\mu D_\mu \psi_i - m_{\psi_i} \bar{\psi}_i \psi_i] - \frac{1}{4} G_{\mu\nu}^a G^{\mu\nu a}, \quad (1)$$

Here, N_f is the number of flavors of dark quarks ψ_i with $i = 1, 2, \dots, N_f$; $D_\mu \psi_i \equiv \partial_\mu \psi_i - i g_d G_\mu^a T^a \psi_i$ with T^a ($a = 1, 2, \dots, N_d^2 - 1$) as the $SU(N_d)$ generators; g_d is the dQCD gauge coupling; and $G_{\mu\nu}^a = \partial_\mu G_\nu^a - \partial_\nu G_\mu^a + g_d f^{abc} G_\mu^b G_\nu^c$ is the dark gluon field tensor. Similar to QCD in the Standard Model (SM), the dQCD gauge coupling becomes nonperturbative at around the dQCD confinement scale Λ_d .

Similar to white dwarfs and at approximately zero temperature, the DQNs have the degenerate Fermi pressure of the dark quarks balanced by the vacuum pressure $B = \Delta P_{\text{vacuum}} =$

$P_{\text{confined}} - P_{\text{unconfined}} \approx \Lambda_d^4$. In the light dark quark mass limit with $m_{\psi_i} \ll \Lambda_d$, the energy density of DQNs is related to the “bag parameter” B by $\rho = 4B$, which provides a relation between the DQN radius and mass

$$R \approx (800 \text{ m}) \left(\frac{M}{M_\odot} \right)^{1/3} \left(\frac{1 \text{ GeV}}{\Lambda_d} \right)^{4/3}. \quad (2)$$

In the above formula we have ignored the gravitational pressure and energy, which is satisfied when $GM \lesssim R$ or when $M \lesssim 0.4 M_\odot (1 \text{ GeV}/\Lambda_d)^2$. The mass per baryon of a DQN is $3^{1/4} \sqrt{2\pi} N_d^{3/4} N_f^{-1/4} \Lambda_d$, which could be lighter than a free dark baryon with a mass proportional to $N_d \Lambda_d$ in the large N_d limit.

On top of the dQCD interaction for the dark quarks, we also introduce an additional long-range DF between two dark (anti-)quarks. For a scalar mediator ϕ , dark quarks have the following Yukawa-type interaction:

$$\mathcal{L}_{\text{Yukawa}} = \frac{1}{2} \partial_\mu \phi \partial^\mu \phi - \sum_i (m_{\psi_i} + y_i \phi) \bar{\psi}_i \psi_i - V_0(\phi), \quad (3)$$

with the potential $V_0(\phi)$ containing the mediator mass term $\frac{1}{2} m_{\text{med}}^2 \phi^2$ as well as other self-interacting terms like $\frac{1}{4} \lambda \phi^4$, which is ignored in this study by assuming a small λ . Further, we consider the ultralight mediator mass regime with the range of the force $1/m_{\text{med}}$ much longer than the DQN radius R , or $1/m_{\text{med}} \gg R$, such that two isolated DQNs could still interact with each other by exchanging ϕ .

We note that the dark quark finite density could modify the vacuum expectation value of the ϕ field inside the DQNs as well as provide a “plasma mass” for the scalar field to suppress the self-potential energy mediated by the scalar force. Including the fermion effective mass, the fermion finite density generates the following effective scalar potential:

$$V_1 = \mathfrak{g} \frac{1}{2\pi^2} \int_0^{k_F} dk k^2 \sqrt{k^2 + (m_\psi + y\phi)^2}, \quad (4)$$

where $\mathfrak{g} = 2N_d N_f$ accounts for dark quark spin, color, and flavor; $m_{\psi_i} = m_\psi$ and $y_i = y$ for simplicity. The Fermi momentum is $k_F^2 = \mu^2 - (m_\psi + y\phi)^2$. Working in the limit of $|m_\psi + y\phi| \ll \mu$, the above integration is approximately

$$V_1 \approx \frac{\mathfrak{g}}{8\pi^2} \mu^2 [\mu^2 - (m_\psi + y\phi)^2]. \quad (5)$$

The leading term multiplied by a factor of $1/3$ provides the leading degenerate Fermi pressure for relativistic fermions. Its balance with the vacuum pressure determines the equilibrium value for the chemical potential as $\mu_{\text{eq}} = (24\pi^2 B/\mathfrak{g})^{1/4}$, which can be used to determine the number density as $n_\psi = \frac{\mathfrak{g}}{6\pi^2} \mu_{\text{eq}}^3$ and the total number of dark quarks as $N_\psi = n_\psi (4\pi R^3)/3$. The term linear in ϕ , proportional to $y m_\psi$, provides a charge density to emit the ϕ field. In the limit of $m_\psi = 0$, the dark quarks are in the fully-occupied chiral fermion states below the Fermi momentum. The emission of a ϕ particle that couples to both left-handed and right-handed fermions is Pauli-blocked.

Note that the scalar effective mass $m_{\text{in}}^2 = \mathfrak{g} y^2 / (4\pi^2) \mu_{\text{eq}}^2$ inside the DQN could be much larger than the free scalar mass m_{med} . An effective mediator mass inside the DQN larger than $1/R$ will

lead to an additional reduction of $1/(m_{\text{in}}R)^2$ for the effective ϕ -charge of the DQN as a result of the screening from the dark quark plasma. This is detailed in Appendix A, where we solve the scalar classical equation of motion with both the source term [the linear term in ϕ in (5)] and the location-dependent effective mass term. Therefore, we consider the parameter region with $|m_{\text{in}}|R < 1$, or

$$y < 2^{19/12} 3^{-7/12} \pi^{5/6} \mathfrak{g}^{-1/4} \Lambda_d^{1/3} M^{-1/3} = (2 \times 10^{-19}) \left(\frac{\Lambda_d}{1 \text{ GeV}} \right)^{1/3} \left(\frac{M_\odot}{M} \right)^{1/3} \left(\frac{\mathfrak{g}}{18} \right)^{-1/4}, \quad (6)$$

where $\mathfrak{g} = 2 \times 3 \times 3$ was chosen similar to ordinary QCD.

The effective “charge” of the DQN coupling to the scalar field is $q_{\text{eff}} y = \frac{\mathfrak{g}}{4\pi^2} m_\psi \mu_{\text{eq}}^2 y \left(\frac{4\pi}{3} R^3 \right) = \frac{3}{2} y \frac{m_\psi}{\mu_{\text{eq}}} N_\psi$, from which the ratio of the “dark force” over the gravitational force between two DQNs is independent of the DQN total masses and is

$$\alpha = \frac{3 \mathfrak{g} y^2 m_\psi^2}{128 \pi^3 G \Lambda_d^4} \lesssim (0.02) \left(\frac{m_\psi/\Lambda_d}{0.5} \right)^2 \left(\frac{1 \text{ GeV}}{\Lambda_d} \right)^{4/3} \left(\frac{M_\odot}{M} \right)^{2/3} \left(\frac{\mathfrak{g}}{18} \right)^{1/2}, \quad (7)$$

for y satisfying (6). If the condition $|m_{\text{in}}|R < 1$ is not satisfied, one could take into account of the additional charge suppression factor of $1/(|m_{\text{in}}|R)^2$ and have the ratio as

$$\alpha = \frac{\left(\frac{\pi}{3} \right)^{1/3} m_\psi^2}{3 \times 2^{2/3} y^2 G \Lambda_d^{8/3} M^{4/3}} \lesssim (0.02) \left(\frac{m_\psi/\Lambda_d}{0.5} \right)^2 \left(\frac{1 \text{ GeV}}{\Lambda_d} \right)^{4/3} \left(\frac{M_\odot}{M} \right)^{2/3} \left(\frac{\mathfrak{g}}{18} \right)^{-1/2}, \quad (8)$$

after using the opposite limit for y in (6). In general, the long-range dark force becomes stronger for a smaller dark confinement scale Λ_d and a lighter DQN mass.

Since the scalar-mediated forces between two fermions, two anti-fermions, or one fermion and one anti-fermion are all attractive, the forces between any DQNs are attractive, regardless whether they are DQNs or anti-DQNs. Because scalar-exchanged long-range forces are coherent, one needs to require the scalar-exchanged potential energy be less than the total mass so as not to change the general features of DQNs compared to the same model without an additional long-range force. The constraint is $y < 4 \times (2/3)^{5/6} 5^{1/2} \pi^{4/3} \mathfrak{g}^{-1/2} (\Lambda_d/m_\psi)(\Lambda_d/M)^{1/3}$, which is less stringent than the constraint in (6).

For the simplified case with the same dark quark masses and Yukawa couplings $m_{\psi_i} = m_\psi$ and $y_i = y$ for all i , the ratio of the effective charge q_{eff} over the DQN mass M is fixed and independent of M in the limit of $|m_{\text{in}}|R < 1$. For a more general case with different values of m_{ψ_i} and y_i , there is a global $U(1)^{N_f}$ flavor symmetry. For a dark quark nugget with total N_ψ dark quark number, the number of dark quarks of each flavor i can be labelled by $(N_{\psi_1}, N_{\psi_2}, \dots, N_{\psi_{N_f}})$ with $\sum_{i=1}^{N_f} N_{\psi_i} = N_\psi$. The effective charge to emit a ϕ particle is $q_{\text{eff}} y(N_{\psi_1}, N_{\psi_2}, \dots, N_{\psi_{N_f}}) = \frac{3}{2} \sum_{i=1}^{N_f} y_i m_{\psi_i} N_{\psi_i} / \mu_{\text{eq}}$. The DQN mass is $M \approx 2^{3/4} 3^{1/4} \pi^{1/2} \mathfrak{g}^{-1/4} \Lambda_d N_\psi$ by ignoring the bare dark quark mass contributions. The ratio of the effective charge over mass is

$$\frac{q_{\text{eff}} y}{M}(N_{\psi_1}, N_{\psi_2}, \dots, N_{\psi_{N_f}}) = \frac{\sqrt{\frac{3}{2}} \sqrt{\mathfrak{g}}}{4\pi \Lambda_d^2} \frac{\sum_{i=1}^{N_f} y_i m_{\psi_i} N_{\psi_i}}{\sum_{i=1}^{N_f} N_{\psi_i}}. \quad (9)$$

So, different flavor-charged dark quark nuggets could have different charge-to-mass ratios.

One formation mechanism of dark quark nuggets has been studied in Ref. [71] based on the first-order phase transition in the dark QCD sector (see also [75–78]). With an initial asymmetric dark baryon number, the average dark baryon number for each nugget is approximately the total number of dark baryons divided by the total number of bubbles within a Hubble volume at the time of phase transition. The existence of the super weak dark force does not affect this formation mechanism. Additionally, depending on the mass difference for the baryons between the true and false vacua, most of the dark quarks may end up either inside or outside of the DQNs. Thus DQNs may make up nearly all of DM, or only a small fraction with free dark baryons dominating the DM energy density.

The second class of models with fermion constituents has a vector boson force mediator, similar to the photon for the electromagnetic force. The Lagrangian contains the mediator mass and interaction terms

$$\mathcal{L}_{\text{vector}} \supset \frac{1}{2} m_{\text{med}}^2 V_\mu V^\mu + g \sum_i \mathbf{q}_i V_\mu \bar{\psi}_i \gamma^\mu \psi_i. \quad (10)$$

The mediator mass m_{med} is much lighter than $1/R$. For simplicity, we assume all dark quarks have the same charge $\mathbf{q}_i = 1$ under the Abelian gauge symmetry and ignore the dark quark masses for this model. Similar to the scalar mediator case, the Fermi finite density generates a screening effect for the static Coulomb charge. The “Debye length” is $\lambda_D = \sqrt{\pi/(2\mathbf{g}g^2)\mu_{\text{eq}}}^{-1}$ [79]. Requiring the Debye length to be longer than the size of the DQN, one has

$$g < 2^{1/12} 3^{-7/12} \pi^{1/3} \mathbf{g}^{-1/4} \Lambda_d^{1/3} M^{-1/3} = (4 \times 10^{-20}) \left(\frac{\Lambda_d}{1 \text{ GeV}} \right)^{1/3} \left(\frac{M_\odot}{M} \right)^{1/3}, \quad (11)$$

with $\mathbf{g} = 2 \times 3 \times 3$. The ratio of the dark long-range force over the gravitational force is

$$\alpha \equiv \frac{\frac{g^2}{4\pi} N_{\psi 1} N_{\psi 2}}{G M_1 M_2} = \frac{\mathbf{g}^{1/2} g^2}{8\sqrt{6}\pi^2 G \Lambda_d^2} < (4.6 \times 10^{-3}) \left(\frac{1 \text{ GeV}}{\Lambda_d} \right)^{4/3} \left(\frac{M_\odot}{M} \right)^{2/3}. \quad (12)$$

The self-interaction potential energy from the Abelian gauge force is less than $M/(60\pi)$ using the constraint in (11) and can be neglected.

Different from the dark scalar force case, the dark gauge charge case is anticipated to produce DQNs with an average gauge charge of zero. Therefore, the formation mechanism from a first-order phase transition leads to a typical nugget net charge due to Poisson fluctuations given by the square root of the average number of dark quarks and anti-quarks in a volume determined by the bubble nucleation separation. This results in a smaller charge-over-mass ratio compared to the case of an initial charge asymmetry as was possible for the scalar charge. However, there could exist also dark electrons that are not charged under dQCD but are charged under the Abelian gauge group. The dark electrons can neutralize the Abelian gauge charge of dark baryons, similar to the situation of the ordinary electrons and protons. Depending on the dark electron mass and gauge coupling, the Bohr radius of the dark electron could be much longer than the dark quark nugget DQN size. Further, the “recombination” temperature of dark electrons could be much lower than the relevant temperature when dark binaries emit the SGWB. With the conditions in the previous two sentences, the DQN can have a larger charge-over-mass ratio

during their mergers, but the DF between two DQNs is repulsive and thus less interesting for producing an enhanced SGWB signal.

Other macroscopic DM models that may admit scalar or vector mediators in a similar way include Q-balls [80–82] (including gauged Q-balls [83–86] or Q-monopole-balls [87]); fermion solitons/fermi-balls [75, 88, 89]; dark nuclei [90–94]; mirror sector objects analogous to ordinary stars, white dwarfs, or neutron stars [95–103]; or dark-charged primordial black holes [104]. Note that charged black holes necessarily have small charge-to-mass ratios for the vector case to avoid a naked singularity, while black holes with scalar hair are not well understood. This makes them less interesting for enhancing the SGWB signal, which we will see requires much larger charge-to-mass ratios. We will treat MDM in a model-independent way in later discussion such that we do not enforce any relation between charge and mass.

3 Dark force mediation and radiation

With the inclusion of the new interaction, the total force between the binary MDM objects takes the form

$$F = -\frac{Gm_1m_2}{r^2} [1 - \alpha e^{-m_{\text{med}}r}(1 + m_{\text{med}}r)] , \quad (13)$$

where α characterizes the strength of the new forces relative to gravity, with $\alpha = -y^2q_1q_2/(4\pi Gm_1m_2)$ in a scalar-mediated model like in (3) or $\alpha = g^2q_1q_2/(4\pi Gm_1m_2)$ in a vector-mediated model like in (10). In principle, α can be either positive or negative, depending on whether the new interaction between the two MDM objects is repulsive or attractive. For binaries to form and merge, $\alpha < 1$ is required so the total force is attractive. We will assume an attractive DF with a negative $\alpha < 0$ in the remainder of the text. We will further assume a massless mediator limit of $m_{\text{med}} \ll r^{-1}$, with which the dark force reduces to an inverse-square law. We therefore parametrize the total force between the binary as $F = -G'm_1m_2/r^2$ where $G' = (1 - \alpha)G \equiv \beta G$ with $\beta > 1$. This leads to a Kepler-like relation

$$\omega^2 = \frac{G'm}{a^3} , \quad (14)$$

with ω as the orbital angular frequency and a as the semimajor axis, and a virial theorem of the total energy

$$E = -\frac{G'm^2\eta}{2a} , \quad (15)$$

where $m = m_1 + m_2$ is the total mass of the binary, and $\eta = m_1m_2/m^2$ is the asymmetry between the two masses. In the massive mediator case $m_{\text{med}} \gg r^{-1}$, G' is replaced by G , recovering the usual gravity-only expressions.

In this work, we employ the purely massless mediator limit. This is valid provided the mediator mass is sufficiently small compared to the binary separation distance and the GW energy spectrum. For the scales relevant here, we expect $r \lesssim \bar{x}$ the average separation between MDM objects at matter-radiation equality, which will be defined in Eq. (24) and is shorter than of order 0.1 pc for the explored model parameter space. This sets an upper bound on the mediator mass of order 6×10^{-23} eV for solar mass MDM, with a less stringent bound for lighter MDM. Another upper bound comes from the GW frequency sensitivities at various

GW observatories. The smallest frequencies are from pulsar timing arrays, which correspond to $f_{\text{GW}} \sim \text{nHz} \sim 7 \times 10^{-25} \text{ eV}$, though the bound is relaxed if only higher frequency observatories are of interest. If the mediator mass is larger than these bounds, then part of the spectrum must be altered, which is a topic for future work. The mediator mass is also bounded from below as a function of the coupling strength α from, *e.g.*, Bullet Cluster constraints on DM self interaction. For the example of $m_{\text{med}} \sim \text{nHz} \sim (10 \text{ pc})^{-1}$, the bound is $\alpha \lesssim 10^8$ to 10^{10} , depending on the DM halo profile assumed [70]. The values of α we consider will easily satisfy all m_{med} constraints discussed here.

From the binary's orbital motion we can derive the GW energy spectrum for a single binary from the binary merger process $dE_{\text{GW}}/f_{\text{GW},s}$, where the subscript $,s$ means the frequency in the source frame (*i.e.*, emitted by the binary). The frequency of the GWs emitted from the binary $f_{\text{GW},s}$ is related to the binary orbital frequency f_{orb} by $f_{\text{GW},s} = 2f_{\text{orb}} = \omega/\pi$.¹ The GW energy spectrum can then be calculated by the chain rule as

$$\frac{dE_{\text{GW}}}{df_{\text{GW},s}} = \frac{\dot{E}_{\text{GW}}}{\dot{f}_{\text{GW},s}} = \frac{\pi \dot{E}_{\text{GW}}}{\dot{\omega}} = \frac{\pi \dot{E}_{\text{GW}}}{-\frac{3\sqrt{2}}{G'm^{5/2}\eta^{3/2}} \sqrt{-\dot{E}\dot{E}}}, \quad (16)$$

where the dots indicate derivatives with respect to time, and the last equality uses Eqs. (14) and (15) to transfer the time derivative on ω to that on the binary system's energy E . Note that the \dot{E}_{GW} in the numerator is the energy emission rate through GWs, while $-\dot{E}$ is the emission rate of the binary system's total energy, to which both GW and DF emission contribute. In other words, $-\dot{E} = \dot{E}_{\text{GW}} + \dot{E}_{\text{DF}}$ (where the sign comes from $\dot{E} < 0$ referring to the loss of energy in the binary, whereas $\dot{E}_{\text{GW},\text{DF}} > 0$ refer to the energy emitted as radiation). Specifically, if the DF emission is negligible then $-\dot{E} \approx \dot{E}_{\text{GW}}$, and without any knowledge on the form of \dot{E}_{GW} the well-known spectral form [106] is obtained:

$$\frac{dE_{\text{GW}}}{df_{\text{GW},s}} = \frac{\pi^{2/3}}{3} G'^{2/3} m^{5/3} \eta f_{\text{GW},s}^{-1/3}. \quad (17)$$

Note that G' is still present in the expression rather than G , as the dark interaction is still affecting the orbital motion of the binary. This spectrum is valid for $G'm/(a_0^3) < \pi^2 f_{\text{GW}}^2 < G'm/((r_1 + r_2)^3)$, where $r_{1,2}$ are the radii of the MDM objects and a_0 is the initial semimajor axis of the binary. The spectrum at still higher frequencies depends on the details of the MDM (*e.g.*, black holes have a merger and ringdown period after their event horizons cross [107, 108]). For the sake of model independence, we neglect any higher frequencies emitted when two MDM merge, meaning our SGWB spectra will be underestimated and our limits conservative.

More generically, for an eccentric orbit with orbital eccentricity e and semi-major axis a , the GW and DF energy emission rate \dot{E}_{GW} and \dot{E}_{DF} are calculated as

$$\langle \dot{E}_{\text{GW}} \rangle = \frac{32GG'^3\eta^2m^5}{5a^5(1-e^2)^{7/2}} \left(1 + \frac{73}{24}e^2 + \frac{37}{96}e^4 \right), \quad (18)$$

$$\langle \dot{E}_{\text{DF}} \rangle = \frac{GG'^2}{12\pi} \eta^2 m^4 \left(\frac{gq_1}{\sqrt{G}m_1} - \frac{gq_2}{\sqrt{G}m_2} \right)^2 \frac{1}{a^4} \frac{2+e^2}{(1-e^2)^{5/2}}, \quad (19)$$

¹It is well known that binaries with eccentric orbits radiate GWs with all harmonics of the orbital frequency [105], *i.e.*, $f_{\text{GW},s} = n f_{\text{orb}}$. The approach presented here effectively treats all GW emission to be through the $n = 2$ harmonic. We have checked the emission through the other harmonics and found their contributions to be negligible. See Appendix D for more details on the higher-harmonic emission.

For concreteness, (19) assumes a vector mediator as the benchmark new force, but the expression for this and other important quantities for a scalar mediator are essentially the same in the massless mediator limit as described in Appendix B. Note that the evolution of a and e is related. A detailed derivation of the energy emission and the orbital evolution function $a(e)$ is left for Appendix B. For simplicity, in the rest of the text we work in the same mass and opposite charge case, $q_1 = -q_2$ and $m_1 = m_2 = M_{\text{MDM}}$. In this case, the squared difference of the charge-to-mass ratios in (19) is $16\pi|\alpha|$.² Then with simultaneous GW and DF emission, the GW energy spectrum from the binary is

$$\frac{dE_{\text{GW}}}{df_{\text{GW},s}} = \frac{\pi\sqrt{a}(37e^4 + 292e^2 + 96)G'^{3/2}M_{\text{MDM}}^{5/2}}{3\sqrt{2}[10a(1-e^2)(2+e^2)(\beta-1) + (37e^4 + 292e^2 + 96)G'M_{\text{MDM}}]}, \quad (20)$$

where $\beta \equiv G'/G$, the first term in the denominator comes from dE_{EM}/dt , and the second comes from dE_{GW}/dt . In general, we expect the energy spectrum to have a three-stage broken power-law behavior as shown in the left panel of Fig. 1, which we briefly analyze below.

The frequency dependence of $dE_{\text{GW}}/df_{\text{GW},s}$ comes from the binary orbital semi-major axis $a = (2G'M_{\text{MDM}}/(\pi^2 f_{\text{GW},s}^2))^{1/3}$, as well as the dependence of the eccentricity e on a (see, *e.g.*, Eqs. (63) and (71) in the Appendix). When $f_{\text{GW},s}$ is very large, a is small, and the GW emission dominates the EM emission in the denominator of Eq. (20). Thus, $dE_{\text{GW}}/df_{\text{GW},s} \propto \sqrt{a} \propto f_{\text{GW},s}^{-1/3}$ as in (17). Similarly, if the initial value of either a_0 or $(1-e_0)$ is small, GW emission will dominate throughout the binary inspiral (as shown in the right panel of Fig. 1). The GW-dominated regime only appears if β and/or the MDM radii are sufficiently small for GW emission to dominate below the cutoff frequency; the dashed lines in Fig. 1 indicate how the spectrum would continue in the absence of a cutoff.

In the other extreme when $f_{\text{GW},s}$ is very small, the eccentricity is near its initial value, which in practice is likely to be near unity. Although the DF emission dominates the GW emission, $a(1-e^2)$ approaches a constant as suggested by the orbital evolution of the DF-dominated case [see Eq. (71) in Appendix B for details], and the denominator of Eq. (20) is insensitive to $f_{\text{GW},s}$. Again the $f_{\text{GW},s}$ dependence comes mainly from the \sqrt{a} in the numerator, and $dE_{\text{GW}}/df_{\text{GW},s} \propto f_{\text{GW},s}^{-1/3}$.

Between the two extremes, the DF emission dominates the GW emission, but the orbital eccentricity e is only mildly dependent on a . The energy spectrum then behaves as $dE_{\text{GW}}/df_{\text{GW},s} \propto \sqrt{a}/a \propto f_{\text{GW},s}^{1/3}$.

Note that with increasing $\beta \gtrsim 1$, the GW spectrum increases and can exceed the gravity-only GW spectrum (particularly at high frequency). The maximum emission frequency also increases. Both effects are because of the larger orbital frequency from Kepler's law. On the other hand, when $\beta \lesssim 1$, increasing β leads to decreasing GW power, particularly at low frequency. This is because most of the binary's energy is radiated away as DF emission, but there is very little enhancement to the GW power because the orbital frequency is barely changed. These results refer only to individual binaries. To understand the effect of increasing β on the SGWB, one must also account for the change in the merger rate, which is the topic of the next section.

²The scalar dark force mediator case is slightly different. Because the force between two MDM objects is always attractive, q_1 and q_2 are of the same sign, which leads to some mild cancellation for the DF emission. As discussed around Eq. (9), the charge-to-mass ratio is not fixed for DQNs with different dark quark flavor charges. This cancellation just leads some order-one number for $\langle \dot{E}_{\text{DF}} \rangle$ of a particular dark binary.

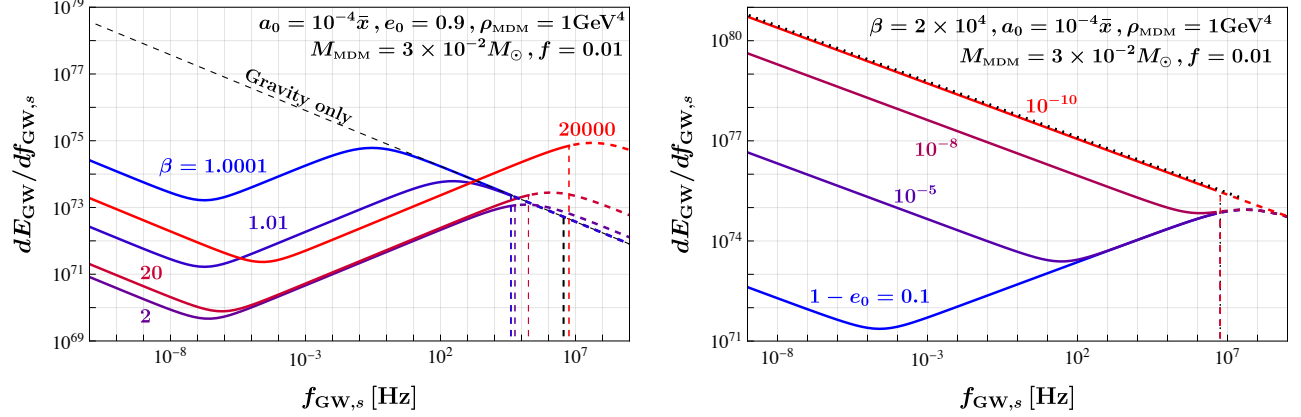


Figure 1: *Left*: The GW energy spectra for various β . The rest of the parameters are chosen as $M_{\text{MDM}} = 3 \times 10^{-2} M_{\odot}$, $e_0 = 0.9$, $f = 0.01$, and $a_0 = 10^{-4} \bar{x}$ where \bar{x} is defined in Eq. (24). The colored vertical dashed lines correspond to the frequency cutoff when the MDMs merge assuming $\rho_{\text{MDM}} = 1 \text{ GeV}^4$, while the dashed curves indicate how the spectrum would continue assuming a still larger ρ_{MDM} . *Right*: The GW energy spectra with $\beta = 2 \times 10^4$ fixed and e_0 varied, with all other parameters the same as the left panel.

4 Merger Rate and Stochastic GW Spectrum

Binaries form predominantly in the early universe before matter-radiation equality [37–39], the ensemble of whose coalescence over time forms the SGWB today. Once the initial distribution of the binaries is given, the merger history can be inferred and the SGWB can be calculated. The case of binary black hole (BBH) mergers has been intensively studied in previous literature [29–31, 34–36], where the SGWB abundance spectrum is calculated as

$$\Omega_{\text{GW}}(f_{\text{GW}}) = \frac{f_{\text{GW}}}{\rho_c H_0} \int_0^{z_{\text{sup}}} dz \frac{R(z)}{(1+z) \sqrt{\Omega_{\text{R}}(1+z)^4 + \Omega_{\text{M}}(1+z)^3 + \Omega_{\Lambda}}} \frac{dE_{\text{GW}}}{df_{\text{GW},s}}(f_{\text{GW},s}) \Big|_{\text{BBH}}, \quad (21)$$

where $R(z)$ is the merger rate at the given redshift z , whose upper integration bound z_{sup} is discussed below after a change of variables; H_0 is the value of the Hubble parameter today; ρ_c is the critical energy density; $\Omega_{\text{R},\text{M},\Lambda}$ denote the abundance of radiation, matter, and dark energy, respectively; and the GW frequency in the source frame $f_{\text{GW},s}$ is related to the observed GW frequency f_{GW} via $f_{\text{GW},s} = (1+z)f_{\text{GW}}$.³ The merger rate R is closely related to the initial distribution of the binaries, which therefore should rely on multiple dynamic variables in principle. The reason why the integration in (21) involves only the frequency (which is closely related to the merger lifetime) is that the gravity-only GW energy spectrum of binary MDM coalescence $dE_{\text{GW}}/df_{\text{GW},s}$ depends only on redshift [107, 108], and thus all the other variables are can be implicitly marginalized. For the case where a dark force is involved, on the other

³This relationship between f_{GW} and $f_{\text{GW},s}$, while standard in the literature, is an approximation. It assumes that the GW frequency spectrum is uniformly redshifted with the reference redshift given by the merger redshift. However, smaller frequencies are emitted earlier and actually redshifted more. Nevertheless, this is a reasonable approximation because the time the binary spends at larger frequencies is significantly shorter than the time it spends at smaller frequencies.

hand, the dynamics and the energy spectrum is more complicated as is shown in the previous section, and we therefore will need to keep all the variables.

In the following, we work in the same-mass opposite-charge case. The merger rate R per unit comoving volume for a given geometry is related to the binary initial distribution P via

$$R(x, y) = \frac{1}{2} \frac{n_{\text{MDM}}}{2} P = \frac{1}{2} \frac{3H_0^2}{8\pi G} \frac{f \Omega_{\text{DM}}}{2M_{\text{MDM}}} P(x, y), \quad (22)$$

where n_{MDM} is the MDM comoving number density, f is the fraction of DM contained in MDM, and the factor $1/2$ in the front accounts for the positive and negative charges of the MDM (which is present for a vector mediator but should be omitted for a scalar mediator). The variables x and y are the initial comoving distances between two nearest-neighboring MDM objects and from the nearest-neighbor center to the next-nearest-neighbor MDM, respectively. We use the normalized initial distribution P given in [38], which assumes the MDM objects form randomly in space and takes into account the tidal disruption from the next-nearest-neighbor MDM on the binary evolution. Specifically,

$$P(x, y) dx dy = \frac{9x^2 y^2}{\bar{x}^6} e^{-(y/\bar{x})^3} dx dy, \quad (23)$$

where \bar{x} is taken as the average separation between MDM objects at matter-radiation equality given by

$$\bar{x} = \frac{1}{1 + z_{\text{eq}}} \left(\frac{8\pi G M_{\text{MDM}}}{3H_0^2 f \Omega_{\text{DM}}} \right)^{1/3} \approx 0.1 \text{ pc} \left(\frac{M_{\text{MDM}}}{M_{\odot}} \right)^{1/3} \left(\frac{1}{f} \right)^{1/3}. \quad (24)$$

In natural units, $(0.1 \text{ pc})^{-1} \approx 6 \times 10^{-23} \text{ eV}$, which sets the rough condition for treating the dark force as Coulomb-like in the limit $m_{\text{med}} \ll \bar{x}^{-1}$, noting that this limit becomes weaker with decreasing M_{MDM} . The semimajor axis a_0 , semiminor axis b_0 , and eccentricity e_0 of the initial binary orbit can be parametrized as

$$a_0 = \frac{c_1}{\beta} \frac{1}{f} \frac{x^4}{\bar{x}^3}, \quad (25)$$

$$b_0 = c_2 \left(\frac{x}{y} \right)^3 a_0, \quad (26)$$

$$e_0 = \sqrt{1 - \left(\frac{b_0}{a_0} \right)^2}, \quad (27)$$

where c_1 and c_2 are $\mathcal{O}(1)$ constants (denoted as α and β in [38]). We adopt $c_1 = 0.4$ and $c_2 = 0.8$, in alignment with [38]. A binary decouples from the Hubble flow when the mean energy density from its additional interaction is equal to the drag from the radiation energy density, *i.e.*, $G' \bar{\rho}_{\text{MDM}} \equiv G' \cdot f \frac{\rho_{\text{eq}}}{2} \frac{\bar{x}^3 R_{\text{eq}}^3}{x^3 R^3} = G \rho_r$, where R is the scalar factor in the FRW metric and the radiation energy density is $\rho_r = \frac{\rho_{\text{eq}}}{2} \frac{R_{\text{eq}}^4}{R^4}$. This implies the decoupling occurs at $R_{\text{dec}}/R_{\text{eq}} = (\beta f)^{-1} (x/\bar{x})^3 < 1$. The decoupling must be earlier than matter-radiation equality because the average energy density created by a nearest-neighbor MDM pair $\bar{\rho}_{\text{MDM}}$ redshifts like matter, and

thus decreases slower than the cosmic energy density only during radiation domination (RD). As a result, any MDM pair that has not already decoupled during RD will not decouple during matter domination (MD) [37–39]. Further refinements to this calculation which include the effects of clustering and binary disruptions in both the early and late universe, as well as the case of an extended rather than monotonic mass function, can be found in [30, 41–43]. These effects are neglected in this work because they require numerical N-body simulations to estimate, which must be redone in the presence of a DF and is thus beyond the scope of this work. Note that binaries that form at later times are generally expected to have a much smaller merger rate than those that form in the early universe and can therefore be neglected [40].

In practice, it is more convenient to use the initial orbital eccentricity e_0 and the lifetime τ of the binaries to express and evaluate the relevant quantities instead of using x and y . In terms of these variables [using (74) as an approximation for the merger lifetime assuming the emission of the dark force carrier dominates the gravitational emission],

$$a_0 = \left(\frac{4G^2(\beta - 1)\beta M_{\text{MDM}}^2 \tau}{h(e_0)} \right)^{1/3} = \left(\frac{\tau/\bar{\tau}}{h(e_0)} \right)^{1/3} \bar{x}, \quad (28)$$

where

$$\bar{\tau} = \frac{2\pi}{3fG(\beta - 1)\beta H_0^2 M_{\text{MDM}}(1 + z_{\text{eq}})^3 \Omega_{\text{DM}}}, \quad (29)$$

$$h(e_0) = e_0^{-4}(1 - e_0^2)^{5/2} \left(1 - \sqrt{1 - e_0^2} \right)^2. \quad (30)$$

To avoid possible confusion, let $\mathcal{P}(\tau, e_0)$ denote the normalized distribution function after proper change of variable, including the Jacobian for changing the integration variables from those in (23). The SGWB is thus calculated as

$$\Omega_{\text{GW}}(f_{\text{GW}}) = \frac{f_{\text{GW}}}{\rho_c} \int_{\sqrt{1-c_s^2}}^{e_0, \text{max}} de_0 \int d\tau \frac{n_{\text{MDM}}}{4} \mathcal{P}(\tau, e_0) \frac{dE_{\text{GW}}}{df_{\text{GW},s}} [(1 + z(t))f_{\text{GW}}], \quad (31)$$

where $dE_{\text{GW}}/df_{\text{GW},s}$ is the GW energy spectrum Eq. (20), $t(\tau, e_0) = t_{\text{dec}}(\tau, e_0) + \tau$ is the time when the binary merges, and t_{dec} is the cosmic time when a binary with a given initial condition decouples from the Hubble flow. The discussion below Eq. (27) implies the binary decoupling happens at redshift

$$1 + z_{\text{dec}} = \left(\frac{2\pi c_1^3(1 + z_{\text{eq}})}{3H_0^2 G M_{\text{MDM}}(\beta - 1)\Omega_{\text{DM}}} \frac{h(e_0)}{\tau} \right)^{1/4}. \quad (32)$$

Apparently $z_{\text{dec}}(t_{\text{dec}})$ is a monotonously decreasing (increasing) function on both e_0 and τ , and thus $t = t_{\text{dec}} + \tau$ monotonously increases with respect to τ , enabling a one-to-one correspondence between the two quantities.

With Eq. (31) given, we need to find the integration range of τ and e_0 . The integration range of τ is subject to three different constraints which are imposed not only directly on τ but also indirectly on t . The first constraint arises from the cosmological requirement that the binary merges after MDM formation and before today. For the representative model in Sec. 2

and similar models, we may generically expect the formation of MDM happens at a cosmic temperature of $T_{\text{form}} \sim \rho_{\text{MDM}}^{1/4}$ [71, 78], or in other words, at a cosmic redshift of $1 + z_{\text{form}} \sim \rho_{\text{MDM}}^{1/4}/T_{\gamma,0}$. The constraint thus requires $t_{\text{form}} < t < t_0$.⁴

The second constraint arises from the requirement that the binary system decouples from the Hubble flow before matter-radiation equality, which sets $x < (f\beta)^{1/3}\bar{x}$. The fact that $x = (a_0 f \beta \bar{x}^3 / c_1)^{1/4}$ together with Eq. (28) gives an upper bound on τ as

$$\tau < c_1^3 f \beta h(e_0) \bar{\tau}. \quad (33)$$

The third constraint comes from the frequency band of an individual merger event. As explained below (17),

$$\frac{G'm}{a_0^3} < \pi^2 [1 + z(t)]^2 f_{\text{GW}}^2 < \frac{G'm}{(2R_{\text{MDM}})^3}. \quad (34)$$

As redshift $z(t)$ is a monotonically decreasing function of t , the right-hand (RH) inequality implies a lower bound of t . The left-hand (LH) inequality is more tricky due to the τ -dependence of a_0 , as given in Eq. (28). Collecting all the t - and τ -dependent terms, the LH inequality is translated to

$$\implies [1 + z(t)]^2 \tau > \frac{1}{\pi^2 f_{\text{GW}}^2} 2G' M_{\text{MDM}} \bar{x}^{-3} \bar{\tau} h(e_0). \quad (35)$$

For any given e_0 the right-hand side (RHS) of (35) evaluates to a constant, while the left-hand side (LHS) could be rather complicated. If t is deep inside the RD regime of the cosmic history (*i.e.*, t and τ are rather small), then we expect $t_{\text{dec}} = \sqrt{\tau}/(2H_0\sqrt{\Omega_{\text{R}}}\mathcal{C}^2)$ where \mathcal{C} is defined through Eq. (32) as $1 + z_{\text{dec}} = \mathcal{C}/\tau^{1/4}$. Then the LHS evaluates to

$$[1 + z(t)]^2 \tau = \frac{\tau}{2H_0\sqrt{\Omega_{\text{R}}} \left(\tau + \frac{\sqrt{\tau}}{2H_0\sqrt{\Omega_{\text{R}}}\mathcal{C}^2} \right)}, \quad (36)$$

which is an increasing function of τ . Meanwhile, for larger τ , we generically have $t \approx \tau$ and the LHS reduces to the monotonous decreasing function $[1 + z(\tau)]^2 \tau$. In other words, the LH inequality of Eq. (34) may impose not only an upper bound on t (or equivalently, τ) but also a lower bound as well.

For the range of the e_0 integration, the lower bound is determined by the requirement $y > x$ [38], *i.e.*, by definition the next-nearest-neighbor MDM object should be further away. With $y = x c_2^{1/3} (1 - e_0^2)^{-1/6}$ this requirement is translated to $e_0 > \sqrt{1 - c_2^2}$. The upper bound on e_0 , $e_{0,\text{max}}$, is determined by the phase space of the τ -integration. Note that it is not guaranteed that there is always a valid phase space for the τ integration under the three constraints described above. In fact, the allowed range of τ decreases as $e_0 \rightarrow 1$ and eventually vanishes completely, which thus determines $e_{0,\text{max}}$ in Eq. (31).

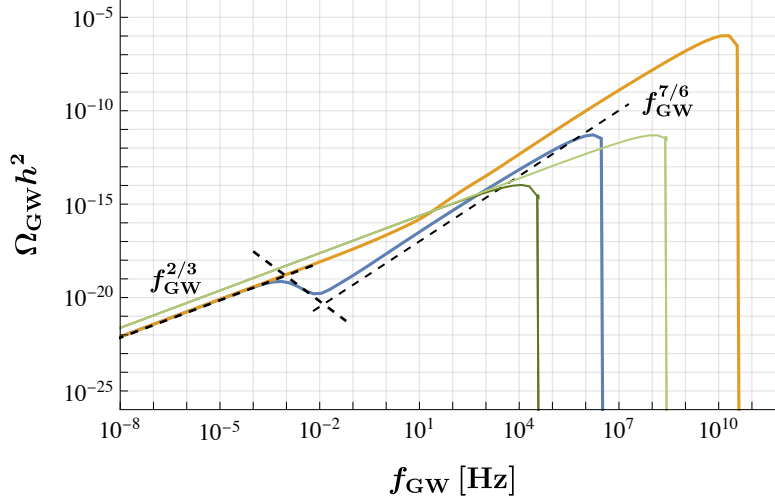


Figure 2: An illustration of the shape of the SGWB from dark binaries. For concreteness, the two curves are calculated with $M_{\text{MDM}} = 10^{-7} M_{\odot}$, $f = 0.01$, $\beta = 10^4$, and $\rho_{\text{MDM}} = 1 \text{ GeV}^4$ (blue, lower) or $(100 \text{ GeV})^4$ (orange, upper), respectively. Also overlaid as dashed lines are the analytic estimates for the blue curve’s power-law behavior given in Eqs. (38), (41), and (97). For comparison, the solid green curves show the spectrum for the gravity-only case, where the darker/lighter green curves share the same M_{MDM} , f , and ρ_{MDM} as the blue/orange curves, respectively. The dark binaries have a larger f_{GW} cutoff when having an attractive DF between them, as the the orbital frequency is increased by the DF.

5 Properties of and constraints on the SGWB

5.1 An analytic understanding of the SGWB spectrum

Due to the complexity of the energy spectrum at the source $dE_{\text{GW}}/df_{\text{GW},s}$, the SGWB behaves as a two- or three-stage broken power-law following the energy spectrum behavior in (1). See Fig. 2 for an illustration, which plots numerical calculations and analytic estimates for $\Omega_{\text{GW}} h^2(f_{\text{GW}})$ with $h = H_0/(100 \text{ km/s/Mpc}) = 0.678$ [109]. Below we will briefly discuss the shape of Ω_{GW} at low and high frequencies, and leave the detailed analytic calculations (including the middle frequencies) for Appendix C.

In the low f_{GW} region, the SGWB is dominated by mergers that largely happen when the universe is radiation dominated, and the orbital eccentricity is largely not softened from one. This is because most binaries merge with very short lifetimes, and all binaries with sufficiently large initial semimajor axis contribute to the low-frequency SGWB (as opposed to the high-frequency background, which due to redshift comes exclusively from more recent mergers). In this regime $t_{\text{dec}} \gg \tau$, *i.e.*, the binaries merge swiftly after their decoupling. For a given merger to contribute a particular GW frequency f_{GW} to the GW spectrum today, it must merge sufficiently late so that the maximum frequency at the source is not redshifted away. From the RH inequality in (34) and the expression in (32) with $t \approx t_{\text{dec}}$, there is a corresponding lower bound on τ for

⁴Binaries that have not yet merged would also contribute to the stochastic GW background.

the integration in (31) given by

$$\tau_{\min} \approx \left(\frac{3\pi f_{\text{GW}}^2}{G' \rho_{\text{MDM}}} \right)^2 \frac{2\pi c_1^3 (1 + z_{\text{eq}}) h(e_0)}{3H_0^2 G M_{\text{MDM}} (\beta - 1) \Omega_{\text{DM}}}. \quad (37)$$

Also, in this frequency regime there will be a competition between the contribution to the spectrum from the GW radiation and the DF radiation at different values of e_0 . At relatively small e_0 the DF emission is more efficient, while above a certain threshold $e_0 > e_{0,\text{th}}$ the GW emission dominates. The latter turns out to make up the majority of the spectrum such that effectively we only need to perform the e_0 -integration on the interval, $[e_{0,\text{th}}, 1)$. The determination of $e_{0,\text{th}}$ is discussed in Appendix C. Both the τ - and the e_0 -integration can be done analytically after these approximations, evaluating to a spectrum of

$$\Omega_{\text{GW}} \approx \left(\frac{85^6 \pi^8 \Gamma^9(\frac{7}{3}) f^{18} G^{14} \beta^{17} H_0^4 M_{\text{MDM}}^{14} (1 + z_{\text{eq}}) \Omega_{\text{DM}}^{17}}{2^{77} 3^4 c_1^{12} c_2^{12} (\beta - 1)^6} \right)^{\frac{1}{15}} f_{\text{GW}}^{2/3}. \quad (38)$$

Note that this result is independent of ρ_{MDM} , which matches the numeric result in Fig. 2. This is as expected: low-frequency GWs should not depend on ρ_{MDM} , which sets the high-frequency cutoff in the binary source frame in $dE_{\text{GW}}/df_{\text{GW},s}$.

In the high frequency regime close to the spectrum cutoff the dominant contribution changes. This regime primarily receives contributions to the SGWB from binaries that satisfy $\tau \gg t_{\text{dec}}$ such that $t \approx \tau$ with binary coalescence occurring during MD. As a result, the orbital eccentricity has had time to soften, and to reasonable approximation $e = 0$. The DF emission dominates the GW emission, leading to

$$1 + z(t) \approx \left(\frac{2}{3H_0 \sqrt{\Omega_{\text{M}} \tau}} \right)^{2/3}, \quad (39)$$

$$\frac{dE}{df_{\text{GW},s}} \approx \left(\frac{2}{3H_0 \sqrt{\Omega_{\text{M}} \tau}} \right)^{2/9} \frac{4 \times 2^{1/3} \pi^{4/3} G'^{4/3} M_{\text{MDM}}^{7/3} f_{\text{GW}}^{1/3}}{5(\beta - 1)}. \quad (40)$$

The inner τ -integration in Eq. (31) can then be evaluated analytically, and the outer e_0 -integration can be done with a saddle-point approximation, which gives

$$\Omega_{\text{GW}} \approx \frac{4 \times 2^{\frac{5}{6}} 13^{\frac{1}{18}} \pi^{\frac{59}{36}} f^{\frac{13}{9}} G^{\frac{55}{36}} \beta^{\frac{67}{36}} (1 + z_{\text{eq}})^{\frac{1}{3}} \rho_{\text{MDM}}^{\frac{1}{12}} H_0^{\frac{1}{9}} M_{\text{MDM}}^{\frac{13}{9}} \Omega_{\text{DM}}^{\frac{10}{9}}}{45 \times 3^{7/36} e^{13/9} c_1^{1/3} c_2^{5/9} (\beta - 1)^{8/9} \Omega_{\text{M}}^{1/18}} f_{\text{GW}}^{7/6}. \quad (41)$$

This also provides a good match to the numeric results as illustrated in Fig. 2. Note that the power-law index of 7/6 depends on our underlying MD assumption. (Assuming RD changes the index to 11/9 with minimal change to the amplitude, which we discuss in Appendix C.) Noticing that the frequency cut-off in the spectrum is determined by maximum frequency of the binary system merging at present, *i.e.*, the upper limit in Eq. (34) taking $z = 0$, the peak frequency and amplitude of the SGWB can be inferred from (41) as

$$f_{\text{GW,max}} = \frac{1}{\pi} \left[\frac{2G' M_{\text{MDM}}}{(2R_{\text{MDM}})^3} \right]^{1/2} = \left(\frac{G' \rho_{\text{MDM}}}{3\pi} \right)^{1/2} = (1 \times 10^6 \text{ Hz}) \left(\frac{\beta}{10^3} \right)^{1/2} \left(\frac{\rho_{\text{MDM}}}{1 \text{ GeV}^4} \right)^{1/2}, \quad (42)$$

$$\Omega_{\text{GW,peak}} \approx \frac{2^{\frac{9}{4}} 13^{\frac{1}{18}} \pi^{\frac{19}{18}} \rho_{\text{MDM}}^{\frac{2}{3}}}{45 \times 3^{\frac{7}{9}} e^{\frac{13}{9}} \Omega_{\text{M}}^{\frac{1}{18}}} \left(\frac{1 + z_{\text{eq}}}{c_1} \right)^{\frac{1}{3}} \left(\frac{f^{13} G^{19} \beta^{22} H_0 M_{\text{MDM}}^{13} \Omega_{\text{DM}}^{10}}{c_2^5 (\beta - 1)^8} \right)^{\frac{1}{9}}. \quad (43)$$

For comparison, the SGWB signal from dark binaries that only couple to gravity without a DF is shown as the green curves in Fig. 2. They are calculated using Eq. (21), with the merger rate $R(z)$ derived from [38]. For some cases, the DF emission can lead to either an enhancement or suppression of the SGWB compared to the gravity-only case. Whether an enhancement or suppression (or both at different frequencies, as for the blue curve) occurs depends on ρ_{MDM} as shown in Fig. 2 as well as β .

There is a subtlety in the calculation of Ω_{GW} near $\Omega_{\text{GW,peak}}$. It can be seen from Eq. (23) that the probability distribution \mathcal{P} in Eq. (31) involves an exponential function, which is explicitly written as

$$\mathcal{P} \propto \exp \left[- \left(\frac{3c_2^4 f^4 \beta^4 (\beta - 1) H_0^2 G M_{\text{MDM}} (1 + z_{\text{eq}})^3 \Omega_{\text{DM}} \tau}{2\pi c_1^3 (1 - e_0^2)^2 h(e_0)} \right)^{1/4} \right]. \quad (44)$$

This exponential function implies that the integration in (31) is strongly influenced by the parameter space where $\tau \sim \tau_{\text{min}}$. If the expression in the exponential is much smaller than -1 even when $\tau \sim \tau_{\text{min}}$, the contribution to Ω_{GW} from the corresponding parameter space should be highly suppressed. In fact, this is related to the validity of the saddle-point approximation we made in the τ -integration in obtaining Eq. (41). Requiring that the expression in the exponential be greater than negative one so that the high frequency spectrum is not suppressed sets a requirement

$$\beta \left(\frac{f}{0.01} \right)^{4/5} \left(\frac{M_{\text{MDM}}}{10^{-10} M_{\odot}} \right)^{1/5} \left(\frac{\tau_{\text{min}}}{t_{\text{now}}} \right)^{1/5} \lesssim 8 \times 10^6 \quad (\text{for no high-frequency suppression}), \quad (45)$$

for $c_1 = 0.4$ and $c_2 = 0.8$. In Fig. 3 we show examples of such suppression when β and f are large. Focusing on β , if β is very large, a vast majority of binaries will merge very early, shortly after forming, and only an exponentially small portion with large initial separations will merge later. The binaries that merge early have their GW signals redshifted, leading to a suppression of the peak frequency. And the larger β becomes, the earlier the binaries merge, leading to larger redshift factors and Ω_{GW} peaking at still smaller frequency. Mathematically, this is captured by the f_{GW} dependence in τ_{min} .

5.2 Experimental sensitivity

5.2.1 Ground- and satellite-based interferometers

The possibility for a SGWB signal $\Omega_{\text{GW}}(f_{\text{GW}})$ to be visible by an experiment is characterized by the signal-to-noise ratio (SNR) ϱ . If ϱ is larger than a threshold value ϱ_{th} then the SGWB can be considered as detectable by the experiment. The sensitivity of the experiment is quantified by the detector noise energy density spectrum $\Omega_{\text{noise}}(f_{\text{GW}})$. If the experiment consists of a single detector, the SNR⁵ is calculated by [110]

$$\varrho = \int df_{\text{GW}} \frac{|h_c(f_{\text{GW}})|^2}{f_{\text{GW}}^2 S_n} = \int df_{\text{GW}} \frac{3H_0^2 \Omega_{\text{GW}}}{2\pi^2 f_{\text{GW}}^4 S_n}, \quad (46)$$

⁵In some works it is ϱ^2 instead of ϱ that is defined with the right hand side of Eq. (46). In that case the SNR is defined with respect to the GW amplitude rather than energy density, see discussions in, *e.g.*, [106]. We use ϱ to remain aligned with the SNR definition (47) from multiple-detector cross-correlation.

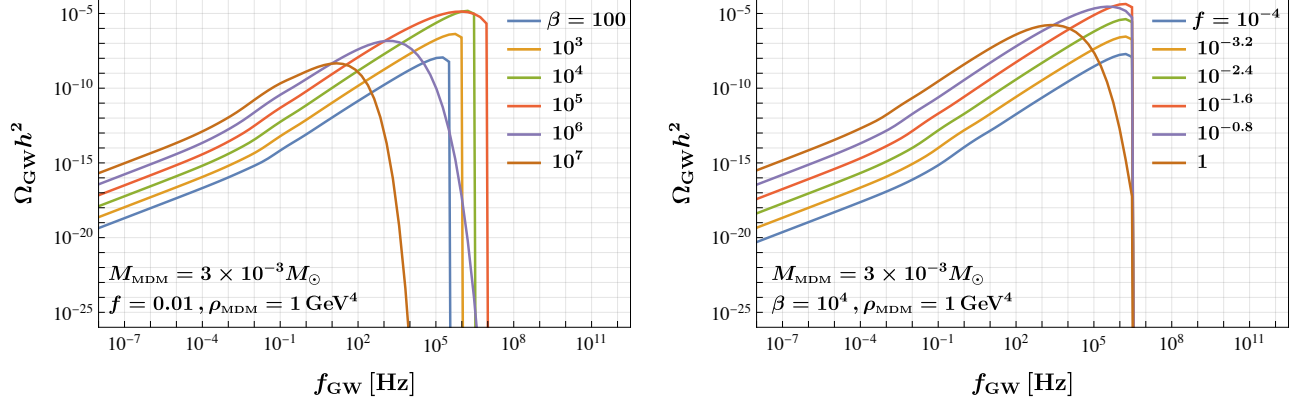


Figure 3: *Left*: The calculated GW spectra for $f = 0.01$ and various β . *Right*: The calculated GW spectra for $\beta = 10^4$ and various f . The rest of the parameters are fixed to be $M_{\text{MDM}} = 3 \times 10^{-3} M_\odot$ and $\rho_{\text{MDM}} = 1 \text{ GeV}^4$. As β and f increase beyond the limit in (45), the amplitude at the predicted peak is severely suppressed and the actual peak is shifted to the lower frequency.

where h_c is dimensionless GW signal strain and S_n is strain noise auto power spectrum of the detector, which is related to the noise energy density spectrum via $\Omega_{\text{noise}} = 2\pi^2 f_{\text{GW}}^3 S_n / (3H_0^2)$. If the experiment contains multiple detectors with uncorrelated noise, the use of the matched filtering technique can greatly improve the sensitivity in a search for a correlated SGWB signal. Then, the SNR is instead calculated as [111]

$$\varrho^2 = n_{\text{det}} T_{\text{obs}} \int df_{\text{GW}} \left(\frac{\Omega_{\text{GW}}}{\Omega_{\text{noise}}} \right)^2, \quad (47)$$

where T_{obs} is the detector's observation time, and $n_{\text{det}} = 2$ for cross-correlation between signals from different detectors. Note that one can repeat the match filtering procedure of cross-correlation, but take all the signals to be from the same detector, which is known as auto-correlation (self-correlation). Applying the match filtering technique in the case of auto-correlation requires either perfect instantaneous noise monitoring or that the noise strain of the detector not be correlated with itself. If this can be achieved then Eq. (47) can be used for a single detector, with n_{det} set to 1.

For the existing and proposed experiments, we mainly consider SKA [19], LISA [18], BBO [20], and the aLIGO-aVirgo network (HLV, HL for the Hanford and Livingston detectors of aLIGO) [14, 112] as the representatives at different frequency bands, among which the cross-correlation technique is applicable on SKA, BBO, and HLV. LISA is a three-satellite Michelson interferometer, and thus is a single detector. We therefore will focus on the SNR calculated from Eq. (46), while we also present results based on an ideal auto-correlation on LISA. Taiji [25] has a configuration close to LISA and a similar noise power spectrum. If it is possible to cross correlate the signals at the two experiments [113], a much better sensitivity can be achieved with matched filtering for GW signals at the mHz frequency range. The observation time T_{obs} is taken as one year for all experiments except SKA, which is taken as 20 years. The threshold SNR is taken to be $\varrho_{\text{th}} = 1$, though the results are not very sensitive to this choice (it is also equivalent to a longer observation time with a higher SNR threshold $\varrho_{\text{th}} = \sqrt{T_{\text{obs}}/(1 \text{ yr})}$, where 1 year would be replaced by 20 years for the case of SKA).

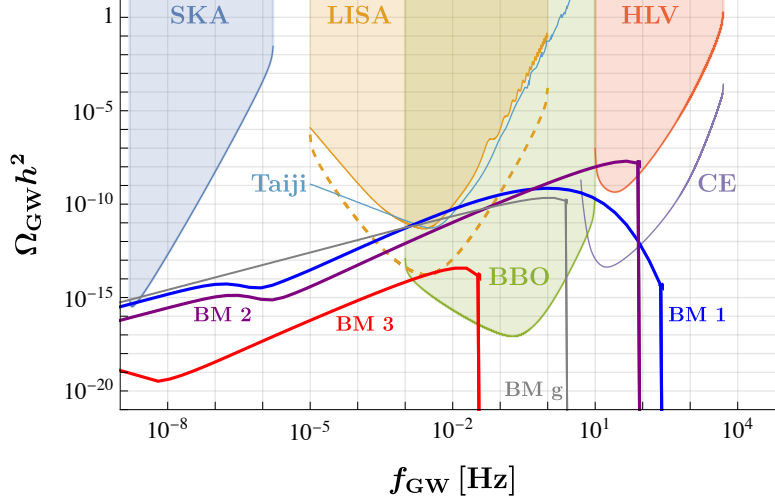


Figure 4: Comparisons between some calculated benchmark SGWB from dark binaries with the PLIS curves of SKA, LISA (dashed), BBO, CE, and HLV and with the noise energy density spectrum Ω_{noise} of LISA (solid) and Taiji. The PLIS of LISA is presented dashed due to the use of auto-correlation. The sensitivity curves are taken from Ref. [111]. Note that the sensitivity curves should only be used as a rough reference of $\varrho_{\text{th}} = 1$ rather than a strict criteria, as discussed in the main text. The model parameters of the three benchmarks BM 1-3 are $(\beta, M_{\text{MDM}}, f, \rho_{\text{MDM}}^{1/4}) = (10^4, 0.1 M_{\odot}, 0.25, 10 \text{ MeV})$, $(10^3, 0.1 M_{\odot}, 0.25, 10 \text{ MeV})$, and $(10^4, 0.1 M_{\odot}, 0.01, 100 \text{ keV})$, respectively, while the gravity-only “BM g” has parameters $(1, 0.1 M_{\odot}, 0.25, 10 \text{ MeV})$ chosen to match those of BM 1 and 2.

In Fig. 4 we show the comparisons between some calculated benchmark (BM) SGWB with the power-law integrated sensitivity (PLIS) $\Omega_{\text{PLIS}} h^2$ of SKA, LISA, BBO, CE [21], and HLV, along with the noise energy density spectra for LISA and Taiji. Note that BM 1, 2, and g are presently excluded by microlensing constraints [50–52, 56, 57] and are presented for illustration only. The PLIS curves and noise energy density spectra are taken from Ref. [111]. Note that these PLIS curves are obtained by assuming the GW signal spectra take the form of an exact power-law, and thus should be used only as references for the experiments’ sensitivities with $\varrho_{\text{th}} = 1$. To correctly account for the experiments’ sensitivities on the parameter space, one still needs to use Eq. (46) or Eq. (47) to calculate the SNR.

The contours of $\varrho = 1$ for SKA, LISA, BBO, and HLV for various β and ρ_{MDM} are shown in Fig. 5, where in the calculation we use the detector Ω_{noise} provided in [111]. On the top row, the SKA constraints do not change much across different panels because the low frequency spectrum (38) is insensitive to ρ_{MDM} . Given the spectral shape, BBO turns out to be the most powerful experiment to search for or constrain the SGWB from the dark binaries. The power-law spectral shape largely implies the contours of constant ϱ to be straight lines, while at large f and β the contours may start to become curved, where the interferometers start to lose sensitivities on the SGWB, as seen in the bottom panels. This is exactly the result of the high-frequency suppression discussed at the end of the previous subsection and illustrated in both Fig. 3 and BM 1 and 2 of Fig. 4. These two BMs illustrate why in the bottom-right panel of Fig. 5 HLV is sensitive to MDM up to $f = 1$ for $\beta = 10^3$ but not for $\beta = 10^4$ —the larger

β of BM 1 leads to a lower frequency cutoff compared to BM 2 in the SGWB spectrum. Also shown in Fig. 5 are the upper bounds on the mass of the MDM assuming the naive dark quark nugget model estimated in Eq. (7) with $\beta = 1 - \alpha > 1$. This bound can be more stringent than the interferometer constraints, especially when ρ_{MDM} is large, but it is model dependent and therefore less universal than the constraints from the interferometer.

It is clear from Figs. 4 and 5 that BBO has the potential to search the widest possible parameter space of all GW interferometers considered here. Clearly, any signal observable by HLV should also be observable by BBO, given the more gradual slope of the Ω_{GW} signal compared to the experimental sensitivities. By the same logic, if a signal is observable at SKA or LISA and has a sufficiently large cutoff frequency, it will also be observed by BBO. In fact, any signal that is visible to any of the other observatories must also be observable by BBO. This may seem counterintuitive—could not a signal be large enough to be visible at LISA or SKA, but then have a small enough cutoff frequency to be invisible to BBO? Indeed, Eqs. (42) and (43) suggest that the peak frequency scales like $\beta^{1/2} \rho_{\text{MDM}}^{1/2}$, and the peak amplitude scales like $\beta^{14/9} \rho_{\text{MDM}}^{2/3}$, so naively it seems like such a possibility can be realized by increasing β and decreasing ρ_{MDM} . For example, in BM 3 in Fig. 4, the parameters $\rho_{\text{MDM}}^{1/4} = 100 \text{ keV}$ and $\beta = 10^4$ result in a peak frequency of the spectrum between 10^{-1} – 10^{-2} Hz , and an amplitude of $\Omega_{\text{GW}} h^2 < 10^{-13}$. A naive calculation suggests that to shift the peak further down by about two orders of magnitude while increasing the amplitude by ~ 10 such that the signal is visible only to LISA auto-correlation we will need $\beta \sim 1 \times 10^8$ and $\rho_{\text{MDM}} \sim (1 \text{ keV})^4$. However, numeric calculations show that with such a large β the peak of the spectrum receives a heavy suppression compared with the naive scaling, as suggested in the end of Sec. 5.1.

5.2.2 High frequency GW signals

In addition to the searches on ground- and satellite-based interferometers, the SGWB is also subject to other constraints from direct searches or indirect observations. In particular, the GWs contribute to the cosmic energy budget as extra radiation degrees of freedom and therefore are constrained by the cosmic microwave background (CMB). The constraint is conventionally parametrized in terms of the number of extra effective neutrino species ΔN_{eff} through

$$\Delta \rho_{\text{rad}} = \frac{\pi^2}{30} \frac{7}{4} \left(\frac{4}{11} \right)^{4/3} \Delta N_{\text{eff}} T^4. \quad (48)$$

The current bounds from CMB measurements are $\Delta N_{\text{eff}} \lesssim 0.3$ [109], and the future CMB-Stage 4 experiment can set a bound of $\Delta N_{\text{eff}} \lesssim 0.06$ at the 95% CL [114]. However, one should not directly compare this constraint with the Ω_{GW} spectrum calculated through (31), because the ΔN_{eff} constraint limits the extra radiation energy budget at recombination, while the Ω_{GW} spectrum from MDM receives a considerable contribution after recombination (similarly, there is no constraint from Big Bang nucleosynthesis). Therefore, to calculate ΔN_{eff} from the dark binaries, the upper integration limit on the binary merger time in (31) must not exceed the time of recombination.

The left panel of Fig. 6 shows a comparison between $\Delta \rho_{\text{rad}} / \rho_{c,0}$ and $\Omega_{\text{GW},0}$ (with subscript ,0 denoting the value today) from both before recombination (dashed) as well as from the whole cosmic history (solid). The spectra of the $\Omega_{\text{GW},0}$ from before recombination can be understood

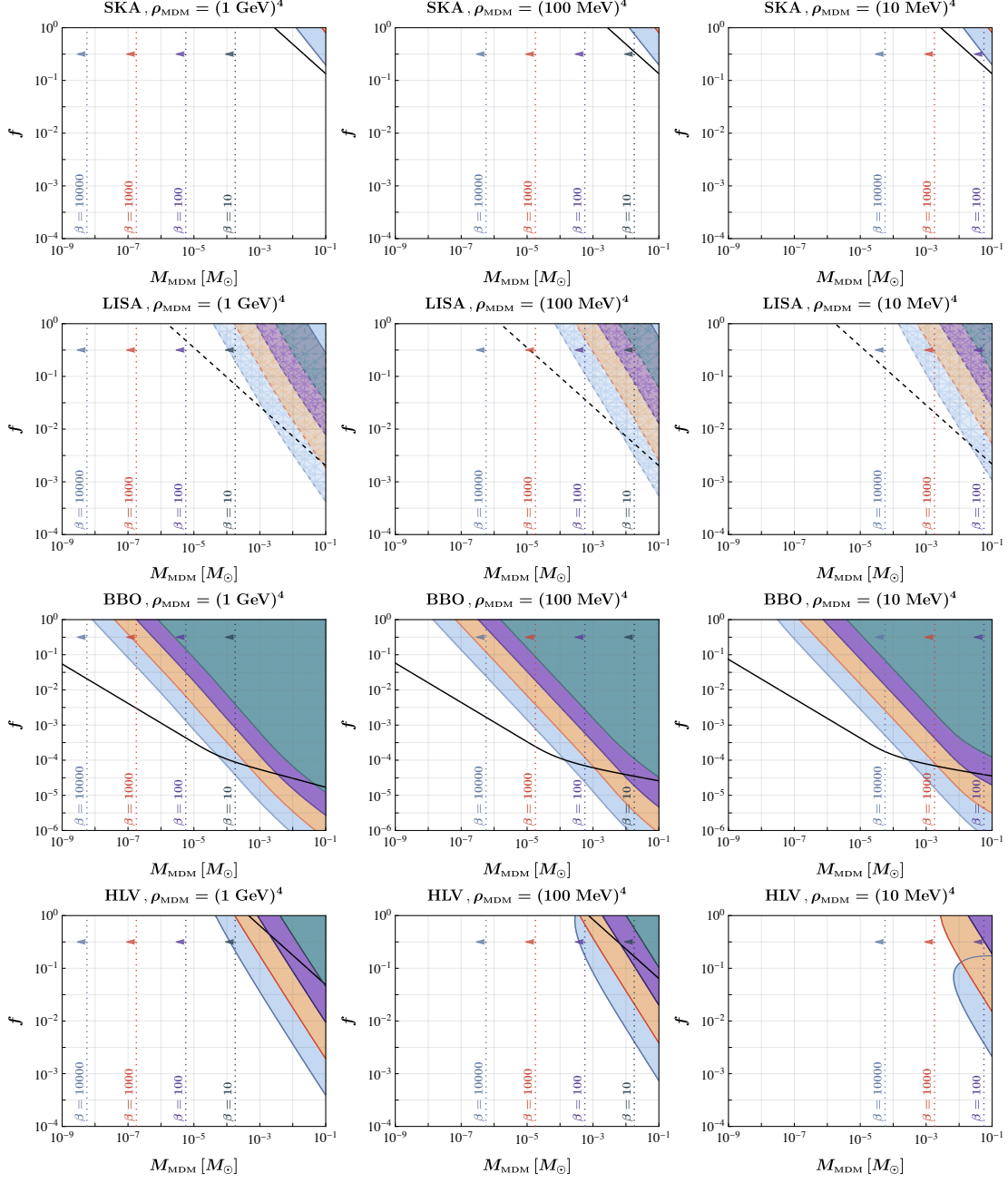


Figure 5: Contours of $\varrho = 1$ of the SGWB from dark binaries on SKA, LISA, BBO, and HLV for various β and MDM densities ρ_{MDM} . The blue/orange/purple/green contours (generally ordered from left to right) are for $\beta = 10000, 1000, 100$, and 10 , respectively, and the values of ρ_{MDM} used are shown above the panels. Black contours refer to the gravity-only case. For LISA (second row), the dashed lines assume a perfect auto-correlation, while the solid lines assume auto-correlation is not applicable. The vertical dashed lines are upper bounds on M_{MDM} for given β assuming the most naive dark quark nugget model, as estimated in Eq. (7). *Note the plot range on the vertical axis is larger for BBO (third row) than for the other observatories.*

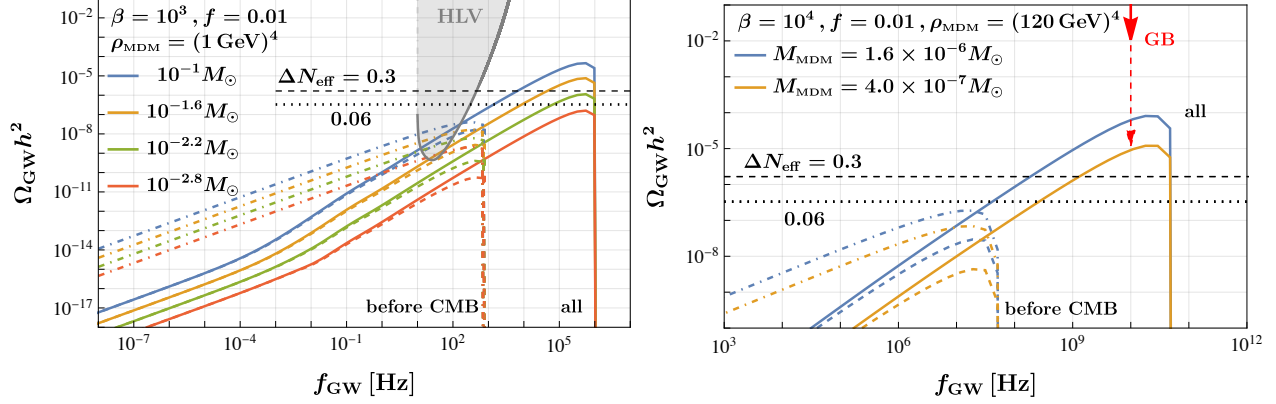


Figure 6: *Left*: The calculated SGWB from contributions only before recombination (dashed) and from all cosmic history (solid), together with the DF radiation before recombination (dot-dashed) for various M_{MDM} . For comparison we show the PLIS curve for the aLIGO-aVirgo network as the gray shaded region, as well as $h^2 \Delta \rho_{\text{rad}} / \rho_{c,0}$ translated from the $\Delta N_{\text{eff}} = 0.3$ and 0.06 bound from the current and expected future CMB measurements as the horizontal lines. Due to the contribution after the recombination, Ω_{GW} today can be larger than $\Delta \rho_{\text{rad}} / \rho_{c,0}$. *Right*: Cases where the SGWB at high frequency can be potentially detected by future Gaussian beam (GB) experiments while remain compatible with the ΔN_{eff} bound at the recombination. The solid red arrow corresponds to $h_c = 10^{-30}$ sensitivity at $f_{\text{GW}} = 10 \text{ GHz}$ in [115], and the dashed red arrow is the projection if the GB strain sensitivity is improved by a factor of 30. The benchmark values are in severe tension with the (model-dependent) upper limits (7) and (12) estimated with dark quark nuggets, while the possibility remains interesting for other models.

as follows. The peak frequency is determined by the maximum GW frequency at the source and therefore is redshifted by $(1 + z_*)$, where $z_* = 1100$ is the redshift at recombination. The amplitude can be checked by performing the same kind of analysis as in Sec. 5.1 by assuming the universe to be RD, which turns out to give a spectrum with very similar amplitude and power-law dependence $f_{\text{GW}}^{11/9}$ at high frequency (see the discussion in Appendix C). Thus the peak amplitude of $\Omega_{\text{GW},0} h^2|_{z_{\text{merge}} > z_*}$ should be about $(1 + z_*)^{11/9}$ smaller than the corresponding $\Omega_{\text{GW},0}$, which roughly matches the numerical results in the figure. As a result, the SGWB from the dark binaries are less constrained by ΔN_{eff} .

In addition to the GW emission, the DF mediator emission also contributes to ΔN_{eff} , which is shown in Fig. 6 as dot-dashed curves. Note that the DF contribution to extra radiation energy dominates the GW contribution at lower frequencies, but they become more comparable at higher frequencies. This is because the binaries have smaller orbital semimajor axes at higher frequencies, so the GW emission becomes more important as illustrated in Eq. (20) and Fig. 1. Note that a calculation of the full constraint involves integrating and adding the whole GW and DF spectra. The relic density of the DF mediator also contributes to ΔN_{eff} , which can be neglected assuming the dark and visible sectors never thermalize and the dark sector is colder than the visible sector.

There are also existing or proposed direct detection experiments hunting for GWs in the MHz-GHz range. See [116–118] for reviews on possible detection approaches and their sensitivities; Ref. [118] in particular discusses SGWBs at high frequencies from primordial BH binaries.

Unfortunately, even if the SGWB from MDM with a long-range DF can partially evade the constraint from ΔN_{eff} , the sensitivity of almost all of these proposed or existing methods are still not good enough to effectively constrain or detect the model parameter space, except for experiments based on the Gaussian beam (GB). A GB consists of a conversion volume with an EM wave continuously propagating along its axis. A GW passing through the GB with a very similar frequency and parallel to the EM wave will convert to EM waves at first order in the GW strain amplitude h_c . This significantly improves upon the GW sensitive compared to other experiments like single photon detection which have conversion probability proportional to h_c^2 . Current GB experimental proposals usually operate at $\mathcal{O}(10)$ GHz and are expected to be sensitive to a GW characteristic strain of $h_c \sim 10^{-30}$ [115, 117]. In Fig. 6 we show the calculated SGWB before CMB and today for two benchmark values of $\rho_{\text{MDM}}^{1/4} = 120$ GeV and $\beta = 10^4$, and compare with the setup of Ref. [115] where the GB is sensitive to a GW strain of $h_c = 10^{-30}$ at $f_{\text{GW}} = 10$ GHz.⁶ Though by far the most promising direct detection method, this GB setup is more than an order of magnitude away from the benchmark points. For the GB setup in Fig. 6 to rule out the $M_{\text{MDM}} = 1.6 \times 10^{-6} M_{\odot}$ benchmark point, it requires an improvement in h_c -sensitivity by (just) a factor of about three, while for the GB proposal in Ref. [117] ($h_c = 4 \times 10^{-29}$ at $f_{\text{GW}} = 40$ GHz) it would be about $\mathcal{O}(100)$. These upgrades could be reasonable in the near future through gyrotron improvements, see the end of Section 4 in [117] for discussions on possible update directions. Thus, GBs may start to rule out some model parameter space where the SGWB is compatible with the ΔN_{eff} and not detectable by the lower-frequency experiments in the previous subsection. On the other hand, more model building is required to understand models that populate this parameter space, since the benchmark points in the right panel of Fig. 6 do not satisfy the model-dependent bounds in (7) and (12), based on the DQN models.

6 Discussion and conclusions

Throughout this work, the nearly massless mediator limit has been assumed. If the mediator mass is increased, it is possible that one or both of $m_{\text{med}} \ll r^{-1}$ or $m_{\text{med}} \ll f_{\text{GW}}$ may be violated for a portion of the inspiral phase of the binary. There are three possible cases to discuss. In the case $f_{\text{GW}} \ll m_{\text{med}} \ll r^{-1}$, the Kepler's law relation is modified, resulting in larger GW emission compared to the gravity-only case, but the DF emission is suppressed. In general, this suppression will lead to a substantially longer merger time than the massless mediator case because GW emission is much slower than DF emission in the massless mediator limit. This is true regardless if $f_{\text{GW,min}} \ll m_{\text{med}} \ll f_{\text{GW,max}}$ or $f_{\text{GW,max}} \ll m_{\text{med}}$ —where $f_{\text{GW,min,max}}$ are the minimum and maximum frequency during the entire inspiral of the binary—because the lifetime is dominated by the lowest-frequency part of the inspiral. These two competing effects—the increased lifetime and suppressed DF emission coupled with enhanced GW emission—must be assessed on a case-by-case basis to determine if the overall SGWB spectrum increases or decreases. In the case $r^{-1} \ll m_{\text{med}} \ll f_{\text{GW}}$, the binary is free to emit DF radiation, but

⁶These benchmark points have densities only a bit below that of black holes at these masses, and they are semirelativistic just before their merger. A full treatment would require a post-Newtonian simulation. This is beyond the scope of this work, and anyways other effects such as the GWs emitted after the merger have also been conservatively neglected due to the model dependence.

the orbital frequency follows the ordinary Kepler’s law determined by gravity. The DF emission leads to a shorter merger time than the gravity-only case, but the GW emission—which depends on the orbital frequency—is not enhanced at all until the orbital radius is sufficiently decreased to feel the attractive DF. Still, because the GW emission is always strongest at late times, if $r_{\text{max}}^{-1} \ll m_{\text{med}} \ll r_{\text{min}}^{-1}$, an enhanced GW emission is possible along with an enhanced merger rate. On the other hand, compared to the massless mediator case, fewer binaries will form, and those that do form will form at later time with larger initial semimajor axis, because the attractive force in the early universe is reduced. Finally, if both $m_{\text{med}} \gg r^{-1}$ and $m_{\text{med}} \gg f_{\text{GW}}$ during a portion or all of the inspiral, the purely gravitational case is recovered. All of these cases require more detailed numerical treatment and are a topic for future work.

In addition to the massless mediator approximation, we have mostly assumed an attractive DF. Compared to the attractive DF assumption $\beta > 1$ or even the gravity-only assumption $\beta = 1$, a repulsive DF with $0 < \beta < 1$ would lead to a decreased GW emission per binary because the orbital frequency in Kepler’s law is reduced and some of the orbital energy may still be emitted as DF radiation. Additionally, it will be harder for MDM objects to find each other and form binaries in the early universe because their attractive force is reduced. This makes a repulsive force less promising for detectability. Another possibility is a repulsive force with $\beta < 0$ but a semi-massive mediator, where the mediator appears massless at longer ranges but massive at shorter ranges (though still longer than MDM radii). Then, binaries could form but would not merge. There would be a most stable distance between the two MDM objects, and as they emit radiation they would eventually come to rest at that position. While this would make for an interesting astrophysical system, clearly the GW emission is suppressed in this case.

In addition to their contribution to the SGWB, individual MDM inspirals or mergers could also be resolved. Indeed, the rate of binary mergers observed by HLVK already sets a constraint in the mass range around $\text{few} \times 10^{-1}$ to $10^3 M_{\odot}$ [43]. With a DF, the merger rate, signal strength, and waveform are also affected (the former two are discussed in this work; for the waveform, see, *e.g.*, [119]). As a result, the bound must be reinterpreted, which is beyond the scope of this work.

We have focused on dark binaries from MDM that forms well before matter-radiation equality. For some MDM models, especially with some interactions in the dark sector similar to the electromagnetic interaction [95–103], the MDM could be formed at a later time after the formation of large scale structure or galaxies. The properties, including the binary merger rates of dark stars or dark planets, are related to the details of the dark interactions. The additional long-range DF could diversify the detectable dark binary systems. For instance, there may be a sizable SGWB that is observable by other proposed high-frequency GW experiments besides the Gaussian beam, while being consistent with the ΔN_{eff} constraints from the CMB observables.

In summary, the presence of a long-range DF substantially modifies the formation, orbital dynamics, evolution, and radiation of MDM binaries due to its contribution to the binding force and addition of a new radiation mode. An attractive DF can increase or decrease the SGWB of merging binaries compared to the gravity-only case. Therefore, dark-charged MDM with planetary to solar masses can be detectable at much smaller abundances than are constrained by microlensing experiments. In particular, GWs at higher frequencies are the most enhanced compared to the gravity-only case, because an attractive force increases the orbital frequency and correspondingly the GW cutoff frequency from mergers. This makes them more detectable not

only at aLIGO-aVIRGO or CE in the Hz-kHz range, but also at very high frequency detectors up to 100 GHz.

Acknowledgments

The authors thank Jeff Dror and Harikrishnan Ramani for useful discussion. The work of YB is supported by the U.S. Department of Energy under the contract DE-SC-0017647. The work of SL is supported by the Area of Excellence (AoE) under the Grant No. AoE/P-404/18-3 issued by the Research Grants Council of Hong Kong S.A.R. The work of NO is partially supported by the National Science Centre, Poland, under research grant no. 2020/38/E/ST2/00243 and by the Arthur B. McDonald Canadian Astroparticle Physics Research Institute. The work of YB was performed in part at Aspen Center for Physics, which is supported by National Science Foundation grant PHY-2210452.

A Dark quark nugget effective charge for the scalar-mediator model

The finite-density effect of the DQNs could generate an in-medium potential for the scalar mediator. This effect could “screen” the effective charge of a DQN to source the scalar field. In this Appendix, we keep a general form of the finite-density potential that contains linear, quadratic, and higher terms in ϕ . To have an analytic calculation, we only keep the linear and quadratic terms. The effective potential is

$$V_{\text{eff}}(\phi) = -a\phi\Theta(R-r) + \frac{1}{2} [m_{\text{in}}^2\Theta(R-r) + m_{\text{med}}^2\Theta(r-R)]\phi^2. \quad (49)$$

Here, $\Theta(x)$ is the Heaviside step function; a is proportional to the fermion number density and the Yukawa coupling; m_{in} is the scalar mass inside the DQN; and m_{med} is the scalar mass outside the DQN (without the medium effect). For a spherical configuration, the classical equation of the scalar mediator is

$$\partial_r^2\phi + \frac{2}{r}\partial_r\phi = \frac{\partial V_{\text{eff}}(\phi)}{\partial\phi}, \quad (50)$$

with the effective potential $V_{\text{eff}}(\phi)$ as a summation of V_0 in (3) and V_1 in (5). Outside the DQN with $m_{\text{med}}^2 > 0$ and the boundary condition $\phi(\infty) = 0$, the solution is $\phi_{\text{out}} = c_1 e^{-m_{\text{med}} r}$. Inside the DQN with $m_{\text{in}}^2 > 0$ and with the Neumann boundary condition $\phi'(r=0) = 0$, the solution is $\phi_{\text{in}} = a/m_{\text{in}}^2 + c_2(e^{-m_{\text{in}} r} - e^{m_{\text{in}} r})/r$. After using the continuity boundary conditions $\phi_{\text{in}}(R) = \phi_{\text{out}}(R)$ and $\phi'_{\text{in}}(R) = \phi'_{\text{out}}(R)$, one has

$$\frac{q_{\text{eff}} y}{4\pi} = c_1 = a \frac{e^{m_{\text{med}} R} [m_{\text{in}} R \cosh(m_{\text{in}} R) - \sinh(m_{\text{in}} R)]}{m_{\text{in}}^2 [m_{\text{med}} \sinh(m_{\text{in}} R) + m_{\text{in}} \cosh(m_{\text{in}} R)]}, \quad (51)$$

$$c_2 = a \frac{m_{\text{med}} R + 1}{2 m_{\text{in}}^2 [m_{\text{in}} \cosh(m_{\text{in}} R) + m_{\text{med}} \sinh(m_{\text{in}} R)]}. \quad (52)$$

In the limit of $m_{\text{in}}R, m_{\text{med}}R \ll 1$, one has $c_1 = a R^3/3$ or $q_{\text{eff}} y = a 4\pi R^3/3$ as anticipated for a spherically symmetric constant source. In the limit with only $m_{\text{med}}R \ll 1$, one has

$$c_1 = a \frac{[m_{\text{in}} R - \tanh(m_{\text{in}} R)]}{m_{\text{in}}^3} \xrightarrow{m_{\text{in}}R \rightarrow \infty} a \frac{R^3}{(m_{\text{in}} R)^2}, \quad (53)$$

which is suppressed by $1/(m_{\text{in}} R)^2$ when the medium-induced scalar mass is much heavier than $1/R$. So, to keep a large effective charge to source the scalar mediator, one may required $m_{\text{in}} R < 1$.

For the case with a negative effective mass inside or $m_{\text{in}}^2 < 0$, one can define $\bar{m}_{\text{in}}^2 = -m_{\text{in}}^2$. The outside solution stays the same, while the inside solution is modified to be $\phi_{\text{in}} = -a/\bar{m}_{\text{in}}^2 + c_2(e^{-i\bar{m}_{\text{in}}r} - e^{i\bar{m}_{\text{in}}r})/r$. After matching the boundary conditions and taking the limit of $m_{\text{med}}R \ll 1$, the formula for c_1 is similar to the previous case with a positive m_{in}^2 and is given by

$$c_1 = -a \frac{[\bar{m}_{\text{in}} R - \tanh(\bar{m}_{\text{in}} R)]}{\bar{m}_{\text{in}}^3} \xrightarrow{\bar{m}_{\text{in}}R \rightarrow \infty} -a \frac{R^3}{(\bar{m}_{\text{in}} R)^2}. \quad (54)$$

B Radiation emission from a binary with a massless dark force mediator

B.1 GW emission

Here, we review the ordinary GW emission from a binary with no additional long-range forces. For further review, see, *e.g.*, [106]. The quadruple radiation depends on the quadruple

$$Q^{ij} \equiv M^{ij} - \frac{1}{3}\delta^{ij}M_{kk}, \quad (55)$$

where the second mass moment

$$M^{ij} = \int d^3x T^{00} x^i x^j, \quad (56)$$

with T^{00} the energy density from the stress-energy tensor. To lowest order in velocity v , $T^{00} \approx \rho$ the mass density. The total radiated quadruple power is then

$$\dot{E}_{\text{GW}} = \frac{G}{5} \langle \ddot{Q}_{ij} \ddot{Q}_{ij} \rangle = \frac{G}{5} \langle \ddot{M}_{ij} \ddot{M}_{ij} - \frac{1}{3}(\ddot{M}_{kk})^2 \rangle, \quad (57)$$

where dots reflect derivatives with respect to time t . For a binary, the radiated power averaged over its orbital period is

$$P_{\text{GW}} = \langle \dot{E}_{\text{GW}} \rangle = \frac{32GG'^3\eta^2m^5}{5a^5(1-e^2)^{7/2}} \left(1 + \frac{73}{24}e^2 + \frac{37}{96}e^4 \right). \quad (58)$$

Note that the single power of G comes from the gravitational coupling for the GW emission, while the other three powers of G' come from the orbital trajectory in the mass density in \ddot{M}_{ij} .

Meanwhile, the angular momentum radiated in quadruple GWs is

$$\dot{L}_{\text{GW}}^i = \frac{2G}{5} \epsilon^{ikl} \langle \ddot{Q}_{ka} \ddot{Q}_{la} \rangle. \quad (59)$$

For a binary, this is

$$\dot{L}_{\text{GW}} = \frac{32GG'^{5/2}\eta^2m^{9/2}}{5a^{7/2}(1-e^2)^2} \left(1 + \frac{7}{8}e^2\right). \quad (60)$$

Consider the time for a binary with initial orbital parameters a_0 and e_0 to merge if GW emission is the dominant/only source of radiation.

To estimate the merger time, first obtain \dot{a} and \dot{e} from \dot{E}_{GW} and \dot{L}_{GW} as [using (15) and $e^2 = 1 + \frac{2EL^2}{G'^2m^5\eta^3}$]

$$\dot{a} = -\frac{2a^2}{G'm^2\eta}\dot{E}_{\text{GW}} = -\frac{64GG'^2\eta m^3}{5a^3(1-e^2)^{7/2}} \left(1 + \frac{73}{24}e^2 + \frac{37}{96}e^4\right), \quad (61)$$

$$\dot{e} = -\frac{\dot{E}_{\text{GW}}L_{\text{GW}}^2 + 2E_{\text{GW}}L_{\text{GW}}\dot{L}_{\text{GW}}}{G'^2m^5\eta^3e} = -\frac{304GG'^2\eta m^3e}{15a^4(1-e^2)^{5/2}} \left(1 + \frac{121}{304}e^2\right). \quad (62)$$

These can be combined to get da/de , which can be integrated analytically to obtain

$$a(e) = a_0 \frac{g(e)}{g(e_0)}, \quad (63)$$

$$g(e) = \frac{e^{12/19}}{1-e^2} \left(1 + \frac{121}{304}e^2\right)^{870/2299}.$$

Noting that $e \rightarrow 0$ as $a \rightarrow 0$, the merger time is obtained from

$$\tau = \int_{e_0}^0 de \left(\frac{de}{dt}\right)^{-1} = \frac{5a_0^4(1-e_0^2)^{7/2}}{256GG'^2\eta m^3} G(e_0), \quad (64)$$

$$G(e_0) = \frac{48}{19g^4(e_0)(1-e_0^2)^{7/2}} \int_0^{e_0} de \frac{g^4(e)(1-e^2)^{5/2}}{e(1 + \frac{121}{304}e^2)}. \quad (65)$$

The function $G(e_0)$ is monotonic in $e_0 \in [0, 1]$ and satisfies $G(0) = 1$ and $G(1) = 768/425$ (note that for the $e \rightarrow 1$ limit, $5/256 \times 768/425 = 3/85$).

B.2 Dark force mediator emission

B.2.1 Vector mediator

The dipole radiation of the massless dark mediator is related to the dipole moment $\mathbf{p} = gq_1\mathbf{x}_1 + gq_2\mathbf{x}_2$

$$\dot{E}_{\text{EM}} = -\frac{2}{3} \frac{1}{4\pi} \ddot{\mathbf{p}}^2 = -\frac{2}{3} G'^2 (gq_1m_2 - gq_2m_1)^2 \frac{1}{r^4}. \quad (66)$$

After time-averaging $1/r^4$ over a period of the orbit, the average energy loss is

$$\begin{aligned} P_{\text{EM}} &= \langle \dot{E}_{\text{EM}} \rangle = \frac{G'^2}{12\pi} (gq_1m_2 - gq_2m_1)^2 \frac{1}{a^4} \frac{2+e^2}{(1-e^2)^{5/2}} \\ &= \frac{GG'^2}{12\pi} \eta^2 m^4 \left(\frac{gq_1}{\sqrt{G}m_1} - \frac{gq_2}{\sqrt{G}m_2} \right)^2 \frac{1}{a^4} \frac{2+e^2}{(1-e^2)^{5/2}}. \end{aligned} \quad (67)$$

For the same-mass opposite-charge case $q_1 = -q_2$ and $m_1 = m_2$, the middle term in the last line (the squared difference in the charge-to-mass ratios) is $16\pi|\alpha|$.

The loss of angular momentum goes as [120],

$$\langle \dot{L}_{\text{EM}} \rangle = \frac{G'^{3/2}(gq_1m_2 - gq_2m_1)^2}{6\pi a^{5/2}(1 - e^2)\sqrt{m}}. \quad (68)$$

As in the GW case [using (15) and $e^2 = 1 + \frac{2EL^2}{G'^2m^5\eta^3}$]

$$\dot{a} = -\frac{2a^2}{G'm^2\eta}\dot{E}_{\text{EM}} = -\frac{GG'}{6\pi}\eta m^2 \left(\frac{gq_1}{\sqrt{G}m_1} - \frac{gq_2}{\sqrt{G}m_2} \right)^2 \frac{1}{a^2} \frac{2 + e^2}{(1 - e^2)^{5/2}}, \quad (69)$$

$$\dot{e} = -\frac{\dot{E}_{\text{EM}}L_{\text{EM}}^2 + 2E_{\text{EM}}L_{\text{EM}}\dot{L}_{\text{EM}}}{G'^2m^5\eta^3e} = -\frac{GG'm^2\eta e}{4\pi a^3(1 - e^2)^{3/2}} \left(\frac{gq_1}{\sqrt{G}m_1} - \frac{gq_2}{\sqrt{G}m_2} \right)^2. \quad (70)$$

These can be combined to obtain da/de , which can be integrated analytically to obtain

$$\begin{aligned} a(e) &= a_0 \frac{g(e)}{g(e_0)}, \\ g(e) &= \frac{e^{4/3}}{1 - e^2}. \end{aligned} \quad (71)$$

Noting that $e \rightarrow 0$ as $a \rightarrow 0$, the merger time is obtained from

$$\tau = \int_{e_0}^0 de \left(\frac{de}{dt} \right)^{-1} \quad (72)$$

$$= \frac{4\pi a_0^3}{GG'\eta m^2} \left(\frac{gq_1}{\sqrt{G}m_1} - \frac{gq_2}{\sqrt{G}m_2} \right)^{-2} \frac{1}{g^3(e_0)} \int_0^{e_0} de \frac{g^3(e)(1 - e^2)^{3/2}}{e} \quad (73)$$

$$= \frac{4\pi a_0^3}{GG'\eta m^2} \left(\frac{gq_1}{\sqrt{G}m_1} - \frac{gq_2}{\sqrt{G}m_2} \right)^{-2} \frac{(1 - e_0^2)^{5/2}(1 - \sqrt{1 - e_0^2})^2}{e_0^4}. \quad (74)$$

The last fraction containing the e_0 goes to $1/4$ as $e_0 \rightarrow 0$.

B.2.2 Scalar mediator

The scalar mediator emission is nearly identical to the vector mediator emission, but both $\langle \dot{E} \rangle$ and $\langle \dot{L} \rangle$ are smaller by a factor of two in the massless mediator limit (see [44] for $\langle \dot{E} \rangle$ and below for $\langle \dot{L} \rangle$). As a result, \dot{e} is smaller by a factor of two compared to Eq. (70), and the lifetime for given initial a_0 and e_0 is larger by a factor of two compared to Eq. (74). The change in lifetime can be absorbed by $\bar{\tau}$ in (29), which would become larger by a factor of two. The expression for $dE_{\text{GW}}/df_{\text{GW}}$ is also increased by a factor of two relative to the EM case when the DF emission dominates, though it is unchanged when GWs dominate. In Ω_{GW} in (31) as well as precursor equations like (22), the $n_{\text{MDM}}/4$ becomes instead $n_{\text{MDM}}/2$ for the case where all MDM carries the same (attractive) scalar charge. Thus, the overall Ω_{GW} integration gives a very similar result for the scalar mediator case as the vector mediator case.

To show the equivalence between the vector and scalar emission we need to show that their emission power \dot{E} and angular momentum loss \dot{L} are the same up to a redefinition of the coupling. It has been shown that with a massless mediator the emission power from the two types of mediators differs by a factor of two [44, 45], and therefore we only need to show that the corresponding \dot{L} differ by the same factor. The angular momentum loss from the vector mediator has been calculated in Ref. [120] in terms of the time derivatives of the dipole, while no result has been given for the scalar mediator, partially due to the not-so-straightforward interpolation. For our purpose, however, we may take a detour and use the formalism in Ref. [44] to show that the angular momentum loss in the vector mediator model is twice as large as the scalar mediator model.

The angular momentum loss is calculated as [120],

$$\dot{L} = \frac{dJ}{dt} = - \int r^2 d\Omega j(\mathbf{r}). \quad (75)$$

We will keep only the leading order terms in the multipole expansion of the source terms, as well as only the leading order $1/r$ terms. For the (real) scalar mediator model, the angular momentum density j is

$$j^i = -\dot{\Phi} \epsilon^{ijk} r^j \partial^k \Phi. \quad (76)$$

Using the approach of [44], we expand the scalar field into Fourier modes as

$$\Phi_{\text{rad}} = \sum_{|n|>n_0} I_n(\hat{r}) \frac{\exp[i(k_n r - n\omega_0 t)]}{r} \equiv \sum_{|n|>n_0} I_n(\hat{r}) \frac{E_n}{r}, \quad (77)$$

where

$$I_n = f_S \int d^3x' \exp(-ik_n \hat{r} \cdot \mathbf{x}') \rho_n(\mathbf{x}'), \quad \rho = \sum_n \rho_n e^{-in\omega_0 t}, \quad (78)$$

with f_S as the effective coupling and \hat{r} the unit vector along the direction of \mathbf{r} , whose derivative and angular integration satisfy

$$\partial^a \hat{r}^b = \frac{1}{r} (\delta^{ab} - \hat{r}^a \hat{r}^b), \quad (79)$$

$$\int d\Omega \hat{r}^a \hat{r}^b = \frac{4\pi}{3} \delta^{ab}, \quad \int d\Omega \hat{r}^a \hat{r}^b \hat{r}^c \hat{r}^d = \frac{4\pi}{15} (\delta^{ab} \delta^{cd} + \delta^{ac} \delta^{bd} + \delta^{ad} \delta^{bc}). \quad (80)$$

Thus,

$$\begin{aligned} \dot{L} &= + \int d\Omega \sum_{|n|,|m|} (-in\omega_0) I_n \epsilon^{ijk} r^j \left((-ik_m) f_S (\partial^k \hat{r}) \cdot \int d^3y' \mathbf{y}' e^{-ik_m \hat{r} \cdot \mathbf{y}'} \rho_m(\mathbf{y}') \right) \langle E_n E_m \rangle \\ &\approx \int d\Omega \sum_{|n|} (-in\omega_0) \left(f_S \int d^3x' (-ik_n \hat{r}^b (x')^b) \rho_n(\mathbf{x}') \right) \epsilon^{ijk} \hat{r}^j \left((ik_n) f_S \int d^3y' (y')^k \rho_{-n}(\mathbf{y}') \right) \\ &= \sum_{|n|>n_0} \frac{4\pi}{3} \left(-in^3 \omega_0^3 \left(1 - \frac{n_0^2}{n^2} \right) f_S^2 \epsilon^{ijk} p_n^j p_{-n}^k \right), \end{aligned} \quad (81)$$

where

$$\mathbf{p}_n = \int d^3x' \mathbf{x}' \rho_n(\mathbf{x}') . \quad (82)$$

Note that for the exponential inside I_n in the first line of (81), we have expanded to leading order, as the total charge is conserved and therefore $\int d^3x' \rho_n$ with $n \neq 0$ vanishes.

For the vector mediator model, the angular momentum density is ⁷

$$j^i = \epsilon^{ijk} (-\partial_0 A_l r_j \partial_k A^l + \partial_l A_0 r_j \partial_k A^l + A_j \partial_0 A_k - A_j \partial_k A_0) . \quad (83)$$

We use the metric $g_{\mu\nu} = \text{diag}\{-1, 1, 1, 1\}$ further on. Again, [44] suggests

$$A^\alpha = \sum_{|n|} I_n^\alpha(\hat{r}) \frac{E_n}{r}, \quad I_n^\alpha(\hat{r}) = f_V \int d^3x' e^{-ik_n \hat{r} \cdot \mathbf{x}'} J_n^\alpha(\mathbf{x}'), \quad (84)$$

where f_V is the gauge coupling and J^α is the current. To the zeroth order,

$$J_n^i(\mathbf{x}') \approx -in\omega_0 (x')^i \rho_n(\mathbf{x}'), \quad I_n^i \approx -in\omega_0 f_V \int d^3x' (x')^i \rho_n(\mathbf{x}') = -in\omega_0 f_V p_n^i . \quad (85)$$

For the zeroth component, Lorentz gauge implies that $I_n^0 = \sqrt{1 - (n_0/n)^2} \hat{r} \cdot \mathbf{I}_n(\mathbf{x}')$ to leading order in $1/r$, and therefore

$$\partial_k A_0 = -\partial_k \left(\sum_{|n|} \sqrt{1 - \left(\frac{n_0}{n}\right)^2} \hat{r}^a I_n^a \frac{E_n}{r} \right), \quad (86)$$

where the negative sign in the first line comes from the metric.

The leading-order contributions to the angular momentum loss in the vector mediator model come from the last two terms in Eq. (83). A straightforward calculation shows that for the third term,

$$\frac{dJ_{(3)}^i}{dt} = - \int r^2 d\Omega \epsilon^{ijk} A_j \partial_0 A_k = \sum_{|n|} 4\pi (-in^3 \omega_0^3 f_V^2 \epsilon^{ijk} p_n^j p_{-n}^k) . \quad (87)$$

For the fourth term,

$$\frac{dJ_{(4)}^i}{dt} = - \int r^2 d\Omega \epsilon^{ijk} (-A_j \partial_k A_0) = \sum_{|n|} \frac{4\pi}{3} \left(in^3 \left(1 - \frac{n_0^2}{n^2} \right) \omega_0^3 f_V^2 \epsilon^{ijk} p_n^j p_{-n}^k \right), \quad (88)$$

where in the derivation we have discarded higher-order terms in $1/r$. Note that the contribution from these two terms are at the zeroth order of the multiple expansion, *i.e.*, taking $e^{-ik_n \hat{r} \cdot \mathbf{x}'} = 1$

⁷Note that the expression in the Appendix of [120] uses temporal gauge while the results in [44] uses Lorentz gauge.

as in Eq. (85). At this order, for the first term of Eq. (83),

$$\begin{aligned} \frac{dJ_{(1)}^i}{dt} &= \int r^2 d\Omega \epsilon^{ijk} \partial_0 A_l r_j \partial_k A^l \\ &= \int d\Omega \sum_{|n|, |m|} \epsilon^{ijk} [(-in\omega_0) I_n^l] r^j \left[f_V \frac{-ik_m}{r} (\delta^{ka} - \hat{r}^k \hat{r}^a) \int d^3 y' (y')^a e^{-ik_m \hat{r} \cdot \mathbf{y}'} J_m^l(\mathbf{y}') \right. \\ &\quad \left. + I_m^l \left(ik_m - \frac{1}{r} \right) \hat{r}^k \right] \langle E_n E_m \rangle. \end{aligned}$$

This entire expression vanishes: the first term in the square brackets contains an odd number of \hat{r} unit vectors and vanishes upon angular integration, while the second term is zero because of the Levi-Civita tensor ϵ^{ijk} . The second term of (83) similarly vanishes. Summing up the (nonzero) third and fourth terms and comparing the summation with Eq. (81) noticing that for a massless mediator $n_0 = 0$ [45]), we see that the angular momentum loss of the vector mediator model is twice of that of the scalar mediator model when $f_S = f_V$.

C More details on the shape of the GW spectra

The GW spectra that we calculate clearly show a change of power-law index across their frequency bands, which we analyze below by checking the behavior of the Ω_{GW} integrand in (31). For concreteness we use the blue curve in Fig. 2 as a benchmark example, which is calculated with $M_{\text{MDM}} = 10^{-7} M_\odot$, $f = 0.01$, $G'/G = 10^4$ and $\rho = 1 \text{ GeV}^4$.

We start from the high frequency regime close to the cut-off of the spectrum, *i.e.*, the $f_{\text{GW}} \gtrsim 10^{-3} \text{ Hz}$ region in our benchmark case. As illustrated in the main text, in this regime the EM emission dominates the GW emission and the orbital eccentricity has been softened from $e \sim 1$. Taking the approximation $t = \tau$ and $e = 0$, assuming matter domination, and ignoring the GW emission term in the denominator of Eq. (20) one has

$$\frac{dE}{df_{\text{GW},s}} \approx \left(\frac{2}{3H_0 \sqrt{\Omega_{\text{M}} \tau}} \right)^{2/9} \frac{4 \times 2^{1/3} \pi^{4/3} G'^{4/3} M_{\text{MDM}}^{7/3} f_{\text{GW}}^{1/3}}{5(\beta - 1)}. \quad (89)$$

Now together with the rest of the terms, the integrand of Eq. (31) has a τ -dependence of $A \tau^{-13/18} e^{-B \tau^{1/4}}$, and the inner τ -integration evaluates to

$$\int_{\tau_{\min}}^{\tau_{\max}} d\tau A \tau^{-13/18} e^{-B \tau^{1/4}} \approx 4AB^{-10/9} \Gamma\left(\frac{10}{9}, B \tau_{\min}^{1/4}\right), \quad (90)$$

$$A = \frac{2^{1/18} 3^{5/18} \pi^{5/6} c_2 (1 + z_{\text{eq}})^{3/2} f^2 \beta^{10/3} G^{11/6} H_0^{7/9} M_{\text{MDM}}^{17/6} \Omega_{\text{DM}}^{1/2}}{5c_1^{3/2} (\beta - 1)^{1/2} \Omega_{\text{M}}^{1/9}} \frac{e_0^3}{(1 - e_0^2)^{11/4} \left(1 - \sqrt{1 - e_0^2}\right)} f_{\text{GW}}^{1/3}, \quad (91)$$

$$B = \frac{3^{1/4} c_2 (1 + z_{\text{eq}})^{3/4} f \sqrt{H_0} \beta (G' - G)^{1/4} M_{\text{MDM}}^{1/4} \Omega_{\text{DM}}^{1/4}}{(2\pi)^{1/4} c_1^{3/4}} \frac{e_0}{(1 - e_0^2)^{9/8} \left(1 - \sqrt{1 - e_0^2}\right)^{1/2}}. \quad (92)$$

We further approximate $\Gamma\left(\frac{10}{9}, z\right) \approx z^{1/9} \exp(-z)$ where $z = B \tau_{\min}^{1/4}$. With this, Eq. (90) is proportional to $(1 - e_0^2)^{-13/8} \exp[-C/(1 - e_0^2)^{9/8}]$ (where C is positive and independent of e_0) and

therefore is peaked at an e_0 very close to one. We can then evaluate the outer integration with respect to e_0 using the saddle-point approximation (after setting powers of e_0 and $1 - \sqrt{1 - e_0^2}$ to 1 and keeping only powers of $1 - e_0^2$). This leads to the expression in Eq. (41)

$$\Omega_{\text{GW,UV}} \approx \frac{4 \times 2^{\frac{5}{6}} \times 13^{\frac{1}{18}} \pi^{\frac{59}{36}} f^{\frac{13}{9}} G^{\frac{55}{36}} \beta^{\frac{67}{36}} (1 + z_{\text{eq}})^{\frac{1}{3}} \rho_{\text{MDM}}^{\frac{1}{12}} H_0^{\frac{1}{9}} M_{\text{MDM}}^{\frac{13}{9}} \Omega_{\text{DM}}^{\frac{10}{9}}}{45 \times 3^{7/36} e^{13/9} c_1^{1/3} c_2^{5/9} (\beta - 1)^{8/9} \Omega_{\text{M}}^{1/18}} f_{\text{GW}}^{7/6},$$

which we refer to as the UV piece of the spectrum. The density ρ_{MDM} is involved through τ_{min} , which in this case is determined by the maximum frequency at the source, *i.e.*, the RHS of the constraint (34). Note that the power-law index of 7/6 depends on our underlying MD assumption. Repeating the exercise above with an RD assumption gives

$$\Omega_{\text{GW}} \approx \frac{4 \times 2^{\frac{11}{18}} \times 13^{\frac{1}{18}} \pi^{\frac{5}{3}} f^{\frac{13}{9}} G^{\frac{3}{2}} \beta^{\frac{11}{6}} (1 + z_{\text{eq}})^{\frac{1}{3}} \rho_{\text{MDM}}^{\frac{1}{18}} H_0^{\frac{1}{9}} M_{\text{MDM}}^{\frac{13}{9}} \Omega_{\text{DM}}^{\frac{10}{9}}}{45 \times 3^{1/18} e^{13/9} c_1^{1/3} c_2^{5/9} (\beta - 1)^{8/9} \Omega_{\text{R}}^{1/18}} f_{\text{GW}}^{11/9}.$$

At smaller f_{GW} , the mergers largely happen when the universe is radiation dominated, and the orbital eccentricity is largely not softened from one. Meanwhile, the binaries merge swiftly after their decoupling, which means that $t_{\text{dec}} \gg \tau$ and

$$\tau_{\text{min}} \approx \left(\frac{3\pi f_{\text{GW}}^2}{G' \rho_{\text{MDM}}} \right)^2 \frac{2\pi c_1^3 (1 + z_{\text{eq}}) h(e_0)}{3H_0^2 G M_{\text{MDM}} (\beta - 1) \Omega_{\text{DM}}}. \quad (93)$$

With these changes, to a good approximation we will take $e = 1$ in Eq. (20) (while note that we make the replacement that $a(1 - e^2) = a_0(e/e_0)^{4/3}(1 - e_0^2)$ from (71) such that the EM process contribution in the denominator doesn't immediately vanish). Then the competition between the EM emission and the GW emission in the denominator of (20) determines the spectral shape. When the EM emission overpowers the GW emission, we may ignore the GW terms in the denominator. Then, with an RD assumption the integrand of (31) behaves like $A\tau^{-3/4}e^{-B\tau^{1/4}}$, and the τ -integration evaluates to

$$\int_{\tau_{\text{min}}}^{\tau_{\text{max}}} d\tau A \tau^{-3/4} e^{-B\tau^{1/4}} = 4AB^{-1} \exp(-B\tau_{\text{min}}^{1/4}), \quad (94)$$

$$A = \frac{85\pi^{\frac{1}{12}} c_2 (1 + z_{\text{eq}})^{17/12} f^2 \beta^{10/3} G^{19/12} H_0^{7/6} M_{\text{MDM}}^{31/12} \Omega_{\text{DM}}^{7/12}}{48 \times 2^{\frac{7}{12}} \times 3^{\frac{5}{12}} c_1^{7/4} (\beta - 1)^{3/4}} \frac{e_0^{10/3}}{(1 - e_0^2)^{25/8} \left(1 - \sqrt{1 - e_0^2}\right)^{1/2}} f_{\text{GW}}^{-1/3}, \quad (95)$$

$$B = \frac{3^{1/4} c_2 (1 + z_{\text{eq}})^{3/4} f \sqrt{H_0} \beta (G' - G)^{1/4} M_{\text{MDM}}^{1/4} \Omega_{\text{DM}}^{1/4}}{(2\pi)^{1/4} c_1^{3/4}} \frac{e_0}{(1 - e_0^2)^{9/8} \left(1 - \sqrt{1 - e_0^2}\right)^{1/2}}. \quad (96)$$

In terms of $(1 - e_0^2)$, Eq. (94) behaves as $(1 - e_0^2)^{-2} \exp[-C/(1 - e_0^2)^{1/2}]$. Performing the outer e_0 -integration with a saddle-point approximation, the GW spectra in this situation is

$$\Omega_{\text{GW,middle}} \approx \frac{85 G^{7/3} \beta^{4/3} H_0^{2/3} M_{\text{MDM}}^{4/3} \Omega_{\text{DM}}^{4/3} \rho_{\text{MDM}}}{3^{5/3} \times 2^{5/6} \pi^{1/6} (1 + z_{\text{eq}})^{4/3} c_1 c_2^2 (\beta - 1)} f_{\text{GW}}^{-4/3}. \quad (97)$$

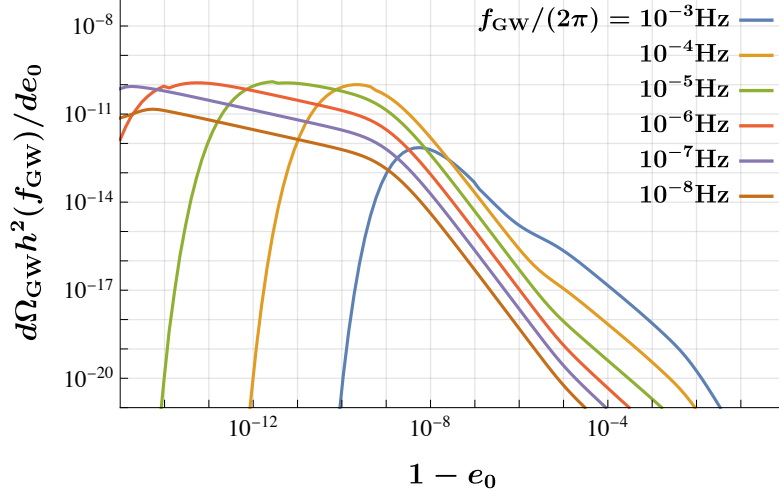


Figure 7: The integrand of the outer e_0 -integration as a function of $1 - e_0$ for various f_{GW} . The horizontal axis is $1 - e_0$, hence $e_0 \rightarrow 1$ to the left. From right to left the curves are for $f_{\text{GW}}/(2\pi) = 10^{-3}, 10^{-4}, \dots, 10^{-8} \text{Hz}$, and the model parameters are the same as the blue curve in Fig. 2. For $f_{\text{GW}}/(2\pi) \lesssim 10^{-5} \text{Hz}$, the integrand starts to have a knee at $1 - e_0 \sim 10^{-9}$, which is due to the competition between the EM and GW emission. At smaller $1 - e_0$ the EM emission dominates.

Note that the power-law index on f_{GW} is now negative, and this corresponds to the region $10^{-3} \text{Hz} \lesssim f_{\text{GW}} \lesssim 10^{-2} \text{Hz}$ of our benchmark point, which we refer to as the middle piece of the spectrum.

At even smaller f_{GW} the competition between the EM emission and GW emission becomes more complicated. Even though the GW emission is the main contributor to Ω_{GW} , it overpowers the EM emission only in the region where e_0 is very close to one. Fig. 7 shows the integrands of the e_0 -integration for various f_{GW} as a function of $1 - e_0$, where there is a knee for most curves around $(1 - e_0) \sim 10^{-9}$, to whose left (where e_0 is closer to 1) the GW emission dominates. In this region the EM emission term in the denominator of (20) may be ignored, and the τ -integration evaluates to

$$\int_{\tau_{\min}}^{\tau_{\max}} d\tau A \tau^{-5/12} e^{-B \tau^{1/4}} = 4A B^{-7/3} \Gamma\left(\frac{7}{3}, B \tau_{\min}^{1/4}\right), \quad (98)$$

$$A = \frac{\pi^{1/12} c_2 (1 + z_{\text{eq}})^{17/12} f^2 \beta^{8/3} (\beta - 1)^{7/12} G^{5/4} H_0^{7/6} M_{\text{MDM}}^{9/4} \Omega_{\text{DM}}^{7/12}}{4 \times 2^{11/12} \times 3^{5/12} c_1^{7/4}} \frac{e_0^{10/3}}{(1 - e_0^2)^{7/6} (1 - \sqrt{1 - e_0^2})^{7/6}} f_{\text{GW}}^{-1/3}, \quad (99)$$

$$B = \frac{3^{1/4} c_2 (1 + z_{\text{eq}})^{3/4} f \sqrt{H_0} \beta (G' - G)^{1/4} M_{\text{MDM}}^{1/4} \Omega_{\text{DM}}^{1/4}}{(2\pi)^{1/4} c_1^{3/4}} \frac{e_0}{(1 - e_0^2)^{9/8} (1 - \sqrt{1 - e_0^2})^{1/2}}. \quad (100)$$

Equating the expressions in (94) and (98) determines the position of the knee, which we denoted $e_{0,\text{th}}$ in the main text. Since we are working in the IR regime where f_{GW} is small, $B \tau_{\min}^{1/4} \ll 1$,

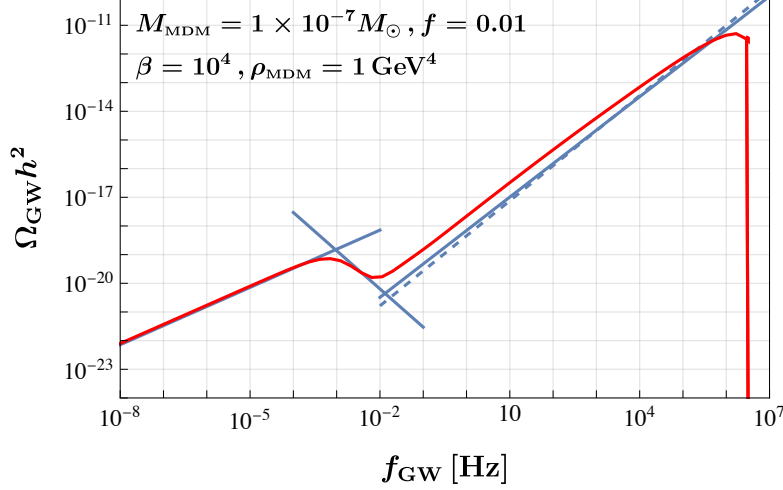


Figure 8: Comparison between our estimated power-law spectra (blue) and numeric results (red). The dashed line assumes radiation domination.

in which case

$$1 - e_{0,\text{th}}^2 = \left(\frac{85 c_2^{4/3} (1 + z_{\text{eq}}) f^{4/3} \beta^2 (G H_0 M_{\text{MDM}})^{2/3} \Omega_{\text{DM}}^{1/3}}{4 \times 3^{2/3} \pi^{1/3} \Gamma(\frac{7}{3}) c_1 (\beta - 1)} \right)^{3/5}. \quad (101)$$

After making the approximation that $\Gamma(\frac{7}{3}, B \tau_{\text{min}}^{1/4}) \approx \Gamma(\frac{7}{3})$ in (98), the integrand has a simple e_0 -dependence of $e_0(1 - e_0^2)^{-1/3}$ that can be integrated analytically. Integrating (98) on the interval $[e_{0,\text{th}}, 1)$ gives the GW spectrum in Eq. (38)

$$\Omega_{\text{GW,IR}} \approx \frac{85^{\frac{2}{5}} \pi^{\frac{8}{15}} [\Gamma(\frac{7}{3})]^{\frac{3}{5}} f^{\frac{6}{5}} (G^{14} \beta^{17} H_0^4 M_{\text{MDM}}^{14} (1 + z_{\text{eq}}) \Omega_{\text{DM}}^{17})^{\frac{1}{15}}}{2^{\frac{77}{15}} 3^{\frac{4}{15}} c_1^{\frac{4}{5}} c_2^{\frac{4}{5}} (\beta - 1)^{\frac{2}{5}}} f_{\text{GW}}^{2/3},$$

which we refer to as the IR piece of the spectrum. The absence of ρ_{MDM} in the expression (as opposed to the UV piece where it is present) is a result of the approximation $\Gamma(\frac{7}{3}, B \tau_{\text{min}}^{1/4}) \approx \Gamma(\frac{7}{3})$. A sanity check of the condition $B \tau_{\text{min}}^{1/4} \ll 1$ using the $e_{0,\text{th}}$ obtained in (101) roughly requires

$$\left(\frac{f_{\text{GW}}}{1 \text{ Hz}} \right) \left(\frac{f}{0.01} \right)^{3/5} \left(\frac{\beta}{10^4} \right)^{1/5} \left(\frac{M_{\text{MDM}}}{M_{\odot}} \right)^{-1/5} \left(\frac{\rho_{\text{MDM}}}{(1 \text{ GeV})^4} \right)^{-1/2} \lesssim 2 \times 10^{12}. \quad (102)$$

A comparison between our calculated power-law spectrum and the numeric results is shown in Fig. 8 (as well as Fig. 2). The analytic estimate is computed in the following way. The IR piece (38) and the middle piece (97) of the spectrum are generated at early times. Both involve a competition between the GW and EM emission, which dominates for the IR and middle piece, respectively. This competition is in the denominator of $dE_{\text{GW}}/df_{\text{GW},s}$, therefore the smaller of the two spectra should be used for the early-time contribution. Meanwhile, the UV piece (41) is generated at late times. Adding the early- and late-time contributions together,

$$\Omega_{\text{GW}}(f_{\text{GW}}) \approx \text{Min}\{\Omega_{\text{GW,IR}}(f_{\text{GW}}), \Omega_{\text{GW,middle}}(f_{\text{GW}})\} + \Omega_{\text{GW,UV}}(f_{\text{GW}}). \quad (103)$$

Some final comments on the competition between the GW process and the EM process in the denominator of $dE/df_{\text{GW},s}$. It can be seen from Eq. (20) that the GW process has a slightly larger power in M_{MDM} , and hence dominates a larger parameter space for heavier MDM. This explains why the middle piece is absent for the spectra of larger M_{MDM} . The same logic suggests that the GW process is more favored when τ_{min} is smaller, which could explain why the middle piece is less significant when ρ_{MDM} is larger, as seen in the two benchmark points in Fig. 2.

D GW emission at higher harmonics

As noted in the main text, our calculation effectively assumes that all the GW emission is through the $f_{\text{GW},s} = 2f_{\text{orb}}$ harmonic, while for a binary with an eccentric orbit the GWs are emitted at all harmonics of the orbital frequency, *i.e.*, $f_{\text{GW},s} = nf_{\text{orb}}$ where n is a positive integer. We have checked that the $n \neq 2$ harmonic channels are not the main contributors to Ω_{GW} . Here we briefly review the formalism to include all harmonics, and then present the results.

The building block of the formalism is the Fourier analysis of the Kepler motion (see, *e.g.*, Section 4.5 of [106] for a review). Since we treat the mediator as massless and hence the binary orbital motion as Kepler-like up to a redefinition of G [see Eq. (14)], the mode decomposition should remain the same. Therefore [105, 121],

$$\frac{dE_{\text{GW}}}{dt} = \frac{32GG'^3\eta^2m^5}{5a^5} \frac{1 + \frac{73}{24}e^2 + \frac{37}{96}e^4}{(1-e^2)^{7/2}} = \frac{32GG'^3\eta^2m^5}{5a^5} \sum_n g(n, e), \quad (104)$$

with

$$g(n, e) = \frac{n^4}{32} \left\{ \left[J_{n-2}(ne) - 2eJ_{n-1}(ne) + \frac{2}{n}J_n(ne) + 2eJ_{n+1}(ne) - J_{n+2}(ne) \right]^2 + (1-e^2) [J_{n-2}(ne) - 2eJ_n(ne) + J_{n+2}(ne)]^2 + \frac{4}{3n^2}J_n^2(ne) \right\}, \quad (105)$$

where $J_n(z)$ is the n -th order Bessel function.

Then,

$$\frac{d^2E_{\text{GW}}}{dt df_{\text{GW},s}} = \frac{32GG'^3\eta^2m^5}{5a^5} \sum_n g(n, e) \delta(f_{\text{GW},s} - nf_{\text{orb}}). \quad (106)$$

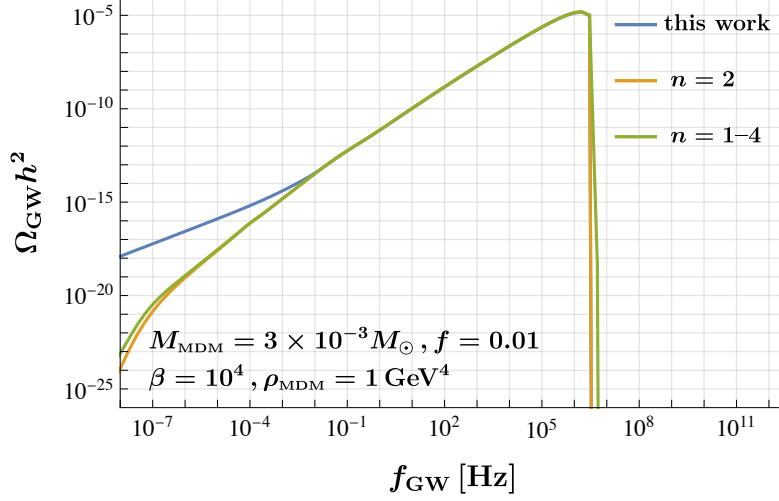


Figure 9: Comparison between the $\Omega_{\text{GW}} h^2$ calculated using our approach and using the harmonic expansion approach in Eq. (107). Our approach agrees very well with the $n = 2$ harmonics which dominates the spectrum in the large f_{GW} regime where EM emission dominates, and can further automatically incorporate the GW emission domination regime at small f_{GW} .

After time integration,

$$\begin{aligned}
\frac{dE_{\text{GW}}}{df_{\text{GW},s}} &= \sum_n \int dt \frac{32GG'^3\eta^2 m^5}{5a^5} g(n, e) \delta(f_{\text{GW},s} - nf_{\text{orb}}) \\
&= \sum_n \int \frac{de}{de/dt} \frac{32GG'^3\eta^2 m^5}{5a^5} g(n, e) \delta(f_{\text{GW},s} - nf_{\text{orb}}) \\
&= \sum_n \int de \frac{32GG'^3\eta^2 m^5}{5a^5} \frac{a^3(1-e^2)^{3/2}}{4eG^2(\beta-1)\beta M_{\text{MDM}}^2} \frac{g(n, e)}{n} \delta(f_{\text{orb}} - f_{\text{GW},s}/n) \\
&= \sum_n \frac{32GG'^3\eta^2 m^5}{5a^5} \frac{a^3(1-e^2)^{3/2}}{4eG^2(\beta-1)\beta M_{\text{MDM}}^2} \frac{g(n, e)}{n} \frac{1}{\left| \frac{df_{\text{orb}}}{de} \right|_{e=e_n}} \quad (107) \\
&\equiv \sum_n \left(\frac{dE_{\text{GW}}}{df_{\text{GW},s}} \right)_n, \quad (108)
\end{aligned}$$

where $e = e_n$ is the root to the equation

$$\frac{f_{\text{GW},s}}{n} = f_{\text{orb}} = \frac{(G'm)^{1/2}}{2\pi a^{3/2}} = \frac{(G'm)^{1/2}}{2\pi} \left(\frac{e_0^{4/3}/(1-e_0^2)}{a_0 e^{4/3}/(1-e^2)} \right)^{3/2}. \quad (109)$$

The energy spectrum $(dE_{\text{GW}}/df_{\text{GW},s})_n$, corresponding to the $dE_{\text{GW}}/df_{\text{GW},s}$ in Eq. (31), can be used to calculate the SGWB from the n -th order harmonic. Fig. 9 shows a comparison between the calculated $\Omega_{\text{GW}} h^2$ using the approach in the main text, along with the $n = 2$ harmonics and the summed $n = 1-4$ harmonics $\Omega_{\text{GW}} h^2$ using Eq. (107). One can see that indeed the $n = 2$ harmonics dominates the contribution, and our approach agrees with the $n = 2$ harmonics very well in the high f_{GW} regime. The deviation in the small f_{GW} region is due to our explicitly

using the orbital evolution results from pure EM emission in (107) and (109), while in the small f_{GW} region we know the GW emission process dominates the spectrum, as analyzed in Sec. 5.1.

References

- [1] **NANOGrav** Collaboration, G. Agazie et al., *The NANOGrav 15 yr Data Set: Evidence for a Gravitational-wave Background*, *Astrophys. J. Lett.* **951** (2023), no. 1 L8, [[arXiv:2306.16213](#)].
- [2] **NANOGrav** Collaboration, G. Agazie et al., *The NANOGrav 15 yr Data Set: Observations and Timing of 68 Millisecond Pulsars*, *Astrophys. J. Lett.* **951** (2023), no. 1 L9, [[arXiv:2306.16217](#)].
- [3] **NANOGrav** Collaboration, A. Afzal et al., *The NANOGrav 15 yr Data Set: Search for Signals from New Physics*, *Astrophys. J. Lett.* **951** (2023), no. 1 L11, [[arXiv:2306.16219](#)].
- [4] **NANOGrav** Collaboration, G. Agazie et al., *The NANOGrav 15 yr Data Set: Constraints on Supermassive Black Hole Binaries from the Gravitational-wave Background*, *Astrophys. J. Lett.* **952** (2023), no. 2 L37, [[arXiv:2306.16220](#)].
- [5] **EPTA** Collaboration, J. Antoniadis et al., *The second data release from the European Pulsar Timing Array - I. The dataset and timing analysis*, *Astron. Astrophys.* **678** (2023) A48, [[arXiv:2306.16224](#)].
- [6] **EPTA, InPTA:** Collaboration, J. Antoniadis et al., *The second data release from the European Pulsar Timing Array - III. Search for gravitational wave signals*, *Astron. Astrophys.* **678** (2023) A50, [[arXiv:2306.16214](#)].
- [7] **EPTA** Collaboration, J. Antoniadis et al., *The second data release from the European Pulsar Timing Array IV. Search for continuous gravitational wave signals*, [arXiv:2306.16226](#).
- [8] **EPTA** Collaboration, J. Antoniadis et al., *The second data release from the European Pulsar Timing Array: V. Implications for massive black holes, dark matter and the early Universe*, [arXiv:2306.16227](#).
- [9] D. J. Reardon et al., *Search for an Isotropic Gravitational-wave Background with the Parkes Pulsar Timing Array*, *Astrophys. J. Lett.* **951** (2023), no. 1 L6, [[arXiv:2306.16215](#)].
- [10] D. J. Reardon et al., *The Gravitational-wave Background Null Hypothesis: Characterizing Noise in Millisecond Pulsar Arrival Times with the Parkes Pulsar Timing Array*, *Astrophys. J. Lett.* **951** (2023), no. 1 L7, [[arXiv:2306.16229](#)].
- [11] A. Zic et al., *The Parkes Pulsar Timing Array Third Data Release*, [arXiv:2306.16230](#).
- [12] H. Xu et al., *Searching for the Nano-Hertz Stochastic Gravitational Wave Background with the Chinese Pulsar Timing Array Data Release I*, *Res. Astron. Astrophys.* **23** (2023), no. 7 075024, [[arXiv:2306.16216](#)].
- [13] **LIGO Scientific, Virgo** Collaboration, B. P. Abbott et al., *Observation of Gravitational Waves from a Binary Black Hole Merger*, *Phys. Rev. Lett.* **116** (2016),

- no. 6 061102, [[arXiv:1602.03837](#)].
- [14] **LIGO Scientific** Collaboration, J. Aasi et al., *Advanced LIGO*, *Class. Quant. Grav.* **32** (2015) 074001, [[arXiv:1411.4547](#)].
 - [15] **LIGO Scientific, Virgo** Collaboration, B. P. Abbott et al., *GWTC-1: A Gravitational-Wave Transient Catalog of Compact Binary Mergers Observed by LIGO and Virgo during the First and Second Observing Runs*, *Phys. Rev. X* **9** (2019), no. 3 031040, [[arXiv:1811.12907](#)].
 - [16] **LIGO Scientific, Virgo** Collaboration, R. Abbott et al., *GWTC-2: Compact Binary Coalescences Observed by LIGO and Virgo During the First Half of the Third Observing Run*, *Phys. Rev. X* **11** (2021) 021053, [[arXiv:2010.14527](#)].
 - [17] **KAGRA, VIRGO, LIGO Scientific** Collaboration, R. Abbott et al., *GWTC-3: Compact Binary Coalescences Observed by LIGO and Virgo during the Second Part of the Third Observing Run*, *Phys. Rev. X* **13** (2023), no. 4 041039, [[arXiv:2111.03606](#)].
 - [18] **LISA** Collaboration, P. Amaro-Seoane et al., *Laser Interferometer Space Antenna*, [arXiv:1702.00786](#).
 - [19] C. L. Carilli and S. Rawlings, *Science with the Square Kilometer Array: Motivation, key science projects, standards and assumptions*, *New Astron. Rev.* **48** (2004) 979, [[astro-ph/0409274](#)].
 - [20] V. Corbin and N. J. Cornish, *Detecting the cosmic gravitational wave background with the big bang observer*, *Class. Quant. Grav.* **23** (2006) 2435–2446, [[gr-qc/0512039](#)].
 - [21] D. Reitze et al., *Cosmic Explorer: The U.S. Contribution to Gravitational-Wave Astronomy beyond LIGO*, *Bull. Am. Astron. Soc.* **51** (2019), no. 7 035, [[arXiv:1907.04833](#)].
 - [22] M. Punturo et al., *The Einstein Telescope: A third-generation gravitational wave observatory*, *Class. Quant. Grav.* **27** (2010) 194002.
 - [23] M. Maggiore et al., *Science Case for the Einstein Telescope*, *JCAP* **03** (2020) 050, [[arXiv:1912.02622](#)].
 - [24] N. Seto, S. Kawamura, and T. Nakamura, *Possibility of direct measurement of the acceleration of the universe using 0.1-Hz band laser interferometer gravitational wave antenna in space*, *Phys. Rev. Lett.* **87** (2001) 221103, [[astro-ph/0108011](#)].
 - [25] W.-R. Hu and Y.-L. Wu, *The Taiji Program in Space for gravitational wave physics and the nature of gravity*, *Natl. Sci. Rev.* **4** (2017), no. 5 685–686.
 - [26] P. Athron, C. Balázs, A. Fowlie, L. Morris, and L. Wu, *Cosmological phase transitions: from perturbative particle physics to gravitational waves*, [arXiv:2305.02357](#).
 - [27] J. Ellis, M. Fairbairn, G. Franciolini, G. Hütsi, A. Iovino, M. Lewicki, M. Raidal, J. Urrutia, V. Vaskonen, and H. Veermäe, *What is the source of the PTA GW signal?*, [arXiv:2308.08546](#).
 - [28] V. Mandic, S. Bird, and I. Cholis, *Stochastic Gravitational-Wave Background due to Primordial Binary Black Hole Mergers*, *Phys. Rev. Lett.* **117** (2016), no. 20 201102, [[arXiv:1608.06699](#)].
 - [29] S. Wang, Y.-F. Wang, Q.-G. Huang, and T. G. F. Li, *Constraints on the Primordial*

- Black Hole Abundance from the First Advanced LIGO Observation Run Using the Stochastic Gravitational-Wave Background*, *Phys. Rev. Lett.* **120** (2018), no. 19 191102, [[arXiv:1610.08725](#)].
- [30] M. Raidal, V. Vaskonen, and H. Veermäe, *Gravitational Waves from Primordial Black Hole Mergers*, *JCAP* **09** (2017) 037, [[arXiv:1707.01480](#)].
 - [31] M. Sasaki, T. Suyama, T. Tanaka, and S. Yokoyama, *Primordial black holes—perspectives in gravitational wave astronomy*, *Class. Quant. Grav.* **35** (2018), no. 6 063001, [[arXiv:1801.05235](#)].
 - [32] O. Pujolas, V. Vaskonen, and H. Veermäe, *Prospects for probing gravitational waves from primordial black hole binaries*, *Phys. Rev. D* **104** (2021), no. 8 083521, [[arXiv:2107.03379](#)].
 - [33] J. García-Bellido, S. Jaraba, and S. Kuroyanagi, *The stochastic gravitational wave background from close hyperbolic encounters of primordial black holes in dense clusters*, *Phys. Dark Univ.* **36** (2022) 101009, [[arXiv:2109.11376](#)].
 - [34] V. Atal, J. J. Blanco-Pillado, A. Sanglas, and N. Triantafyllou, *Constraining changes in the merger history of BH and PBH binaries with the stochastic gravitational wave background*, *Phys. Rev. D* **105** (2022), no. 12 123522, [[arXiv:2201.12218](#)].
 - [35] M. Braglia, J. Garcia-Bellido, and S. Kuroyanagi, *Tracking the origin of black holes with the stochastic gravitational wave background popcorn signal*, *Mon. Not. Roy. Astron. Soc.* **519** (2023), no. 4 6008–6019, [[arXiv:2201.13414](#)].
 - [36] I. K. Banerjee and U. K. Dey, *Probing the origin of primordial black holes through novel gravitational wave spectrum*, *JCAP* **07** (2023) 024, [[arXiv:2305.07569](#)].
 - [37] T. Nakamura, M. Sasaki, T. Tanaka, and K. S. Thorne, *Gravitational waves from coalescing black hole MACHO binaries*, *Astrophys. J. Lett.* **487** (1997) L139–L142, [[astro-ph/9708060](#)].
 - [38] K. Ioka, T. Chiba, T. Tanaka, and T. Nakamura, *Black hole binary formation in the expanding universe: Three body problem approximation*, *Phys. Rev. D* **58** (1998) 063003, [[astro-ph/9807018](#)].
 - [39] M. Sasaki, T. Suyama, T. Tanaka, and S. Yokoyama, *Primordial Black Hole Scenario for the Gravitational-Wave Event GW150914*, *Phys. Rev. Lett.* **117** (2016), no. 6 061101, [[arXiv:1603.08338](#)]. [Erratum: *Phys. Rev. Lett.* 121, 059901 (2018)].
 - [40] Y. Ali-Haïmoud, E. D. Kovetz, and M. Kamionkowski, *Merger rate of primordial black-hole binaries*, *Phys. Rev. D* **96** (2017), no. 12 123523, [[arXiv:1709.06576](#)].
 - [41] M. Raidal, C. Spethmann, V. Vaskonen, and H. Veermäe, *Formation and Evolution of Primordial Black Hole Binaries in the Early Universe*, *JCAP* **02** (2019) 018, [[arXiv:1812.01930](#)].
 - [42] V. Vaskonen and H. Veermäe, *Lower bound on the primordial black hole merger rate*, *Phys. Rev. D* **101** (2020), no. 4 043015, [[arXiv:1908.09752](#)].
 - [43] G. Hütsi, M. Raidal, V. Vaskonen, and H. Veermäe, *Two populations of LIGO-Virgo black holes*, *JCAP* **03** (2021) 068, [[arXiv:2012.02786](#)].
 - [44] D. Krause, H. T. Kloor, and E. Fischbach, *Multipole radiation from massive fields:*

- Application to binary pulsar systems*, *Phys. Rev. D* **49** (1994) 6892–6906.
- [45] S. Alexander, E. McDonough, R. Sims, and N. Yunes, *Hidden-Sector Modifications to Gravitational Waves From Binary Inspirals*, *Class. Quant. Grav.* **35** (2018), no. 23 235012, [[arXiv:1808.05286](#)].
 - [46] J. A. Dror, R. Laha, and T. Opferkuch, *Probing muonic forces with neutron star binaries*, *Phys. Rev. D* **102** (2020), no. 2 023005, [[arXiv:1909.12845](#)].
 - [47] H. Niikura et al., *Microlensing constraints on primordial black holes with Subaru/HSC Andromeda observations*, *Nature Astron.* **3** (2019), no. 6 524–534, [[arXiv:1701.02151](#)].
 - [48] N. Smyth, S. Profumo, S. English, T. Jeltema, K. McKinnon, and P. Guhathakurta, *Updated Constraints on Asteroid-Mass Primordial Black Holes as Dark Matter*, *Phys. Rev. D* **101** (2020), no. 6 063005, [[arXiv:1910.01285](#)].
 - [49] K. Griest, A. M. Cieplak, and M. J. Lehner, *Experimental Limits on Primordial Black Hole Dark Matter from the First 2 yr of Kepler Data*, *Astrophys. J.* **786** (2014), no. 2 158, [[arXiv:1307.5798](#)].
 - [50] **Macho** Collaboration, R. A. Allsman et al., *MACHO project limits on black hole dark matter in the 1-30 solar mass range*, *Astrophys. J. Lett.* **550** (2001) L169, [[astro-ph/0011506](#)].
 - [51] **EROS-2** Collaboration, P. Tisserand et al., *Limits on the Macho Content of the Galactic Halo from the EROS-2 Survey of the Magellanic Clouds*, *Astron. Astrophys.* **469** (2007) 387–404, [[astro-ph/0607207](#)].
 - [52] L. Wyrzykowski, J. Skowron, S. Kozłowski, A. Udalski, M. K. Szymański, M. Kubiak, G. Pietrzyński, I. Soszyński, O. Szewczyk, K. Ulaczyk, R. Poleski, and P. Tisserand, *The ogle view of microlensing towards the magellanic clouds - iv. ogle-iii smc data and final conclusions on machos: The ogle-iii view of microlensing towards the smc*, *Monthly Notices of the Royal Astronomical Society* **416** (Aug., 2011) 2949–2961.
 - [53] H. Niikura, M. Takada, S. Yokoyama, T. Sumi, and S. Masaki, *Constraints on Earth-mass primordial black holes from OGLE 5-year microlensing events*, *Phys. Rev. D* **99** (2019), no. 8 083503, [[arXiv:1901.07120](#)].
 - [54] M. Zumalacarregui and U. Seljak, *Limits on stellar-mass compact objects as dark matter from gravitational lensing of type Ia supernovae*, *Phys. Rev. Lett.* **121** (2018), no. 14 141101, [[arXiv:1712.02240](#)].
 - [55] M. Oguri, J. M. Diego, N. Kaiser, P. L. Kelly, and T. Broadhurst, *Understanding caustic crossings in giant arcs: characteristic scales, event rates, and constraints on compact dark matter*, *Phys. Rev. D* **97** (2018), no. 2 023518, [[arXiv:1710.00148](#)].
 - [56] D. Croon, D. McKeen, and N. Raj, *Gravitational microlensing by dark matter in extended structures*, *Phys. Rev. D* **101** (2020), no. 8 083013, [[arXiv:2002.08962](#)].
 - [57] Y. Bai, A. J. Long, and S. Lu, *Tests of Dark MACHOs: Lensing, Accretion, and Glow*, *JCAP* **09** (2020) 044, [[arXiv:2003.13182](#)].
 - [58] A. Katz, J. Kopp, S. Sibiryakov, and W. Xue, *Femtolensing by Dark Matter Revisited*, *JCAP* **12** (2018) 005, [[arXiv:1807.11495](#)].
 - [59] Y. Bai and N. Orlofsky, *Microlensing of X-ray Pulsars: a Method to Detect Primordial*

- Black Hole Dark Matter*, *Phys. Rev. D* **99** (2019), no. 12 123019, [[arXiv:1812.01427](#)].
- [60] S. Jung and T. Kim, *Gamma-ray burst lensing parallax: Closing the primordial black hole dark matter mass window*, *Phys. Rev. Res.* **2** (2020), no. 1 013113, [[arXiv:1908.00078](#)].
 - [61] M. Ricotti, J. P. Ostriker, and K. J. Mack, *Effect of Primordial Black Holes on the Cosmic Microwave Background and Cosmological Parameter Estimates*, *Astrophys. J.* **680** (2008) 829, [[arXiv:0709.0524](#)].
 - [62] Y. Ali-Haïmoud and M. Kamionkowski, *Cosmic microwave background limits on accreting primordial black holes*, *Phys. Rev. D* **95** (2017), no. 4 043534, [[arXiv:1612.05644](#)].
 - [63] V. Poulin, P. D. Serpico, F. Calore, S. Clesse, and K. Kohri, *CMB bounds on disk-accreting massive primordial black holes*, *Phys. Rev. D* **96** (2017), no. 8 083524, [[arXiv:1707.04206](#)].
 - [64] P. D. Serpico, V. Poulin, D. Inman, and K. Kohri, *Cosmic microwave background bounds on primordial black holes including dark matter halo accretion*, *Phys. Rev. Res.* **2** (2020), no. 2 023204, [[arXiv:2002.10771](#)].
 - [65] T. D. Brandt, *Constraints on MACHO Dark Matter from Compact Stellar Systems in Ultra-Faint Dwarf Galaxies*, *Astrophys. J. Lett.* **824** (2016), no. 2 L31, [[arXiv:1605.03665](#)].
 - [66] S. M. Koushiappas and A. Loeb, *Dynamics of Dwarf Galaxies Disfavor Stellar-Mass Black Holes as Dark Matter*, *Phys. Rev. Lett.* **119** (2017), no. 4 041102, [[arXiv:1704.01668](#)].
 - [67] N. Afshordi, P. McDonald, and D. N. Spergel, *Primordial black holes as dark matter: The Power spectrum and evaporation of early structures*, *Astrophys. J. Lett.* **594** (2003) L71–L74, [[astro-ph/0302035](#)].
 - [68] R. Murgia, G. Scelfo, M. Viel, and A. Raccanelli, *Lyman- α Forest Constraints on Primordial Black Holes as Dark Matter*, *Phys. Rev. Lett.* **123** (2019), no. 7 071102, [[arXiv:1903.10509](#)].
 - [69] S. Savastano, L. Amendola, J. Rubio, and C. Wetterich, *Primordial dark matter halos from fifth forces*, *Phys. Rev. D* **100** (2019), no. 8 083518, [[arXiv:1906.05300](#)].
 - [70] Z. Bogorad, P. W. Graham, and H. Ramani, *Coherent Self-Interactions of Dark Matter in the Bullet Cluster*, [[arXiv:2311.07648](#)].
 - [71] Y. Bai, A. J. Long, and S. Lu, *Dark Quark Nuggets*, *Phys. Rev. D* **99** (2019), no. 5 055047, [[arXiv:1810.04360](#)].
 - [72] G. Krnjaic and K. Sigurdson, *Big Bang Darkleosynthesis*, *Phys. Lett. B* **751** (2015) 464–468, [[arXiv:1406.1171](#)].
 - [73] Y. Bai and A. J. Long, *Six Flavor Quark Matter*, *JHEP* **06** (2018) 072, [[arXiv:1804.10249](#)].
 - [74] X. Liang and A. Zhitnitsky, *Axion field and the quark nugget’s formation at the QCD phase transition*, *Phys. Rev. D* **94** (2016), no. 8 083502, [[arXiv:1606.00435](#)].
 - [75] J.-P. Hong, S. Jung, and K.-P. Xie, *Fermi-ball dark matter from a first-order phase transition*, *Phys. Rev. D* **102** (2020), no. 7 075028, [[arXiv:2008.04430](#)].

- [76] P. Lu, K. Kawana, and K.-P. Xie, *Old phase remnants in first-order phase transitions*, *Phys. Rev. D* **105** (2022), no. 12 123503, [[arXiv:2202.03439](#)].
- [77] K. Kawana, P. Lu, and K.-P. Xie, *First-order phase transition and fate of false vacuum remnants*, *JCAP* **10** (2022) 030, [[arXiv:2206.09923](#)].
- [78] Y. Bai, S. Lu, and N. Orlofsky, *Origin of nontopological soliton dark matter: solitosynthesis or phase transition*, *JHEP* **10** (2022) 181, [[arXiv:2208.12290](#)].
- [79] B. Jancovici, *On the relativistic degenerate electron gas*, *Il Nuovo Cimento* **25** (1962) 428.
- [80] G. Rosen, *Particlelike Solutions to Nonlinear Complex Scalar Field Theories with Positive-Definite Energy Densities*, *J. Math. Phys.* **9** (1968) 996.
- [81] R. Friedberg, T. D. Lee, and A. Sirlin, *A Class of Scalar-Field Soliton Solutions in Three Space Dimensions*, *Phys. Rev. D* **13** (1976) 2739–2761.
- [82] S. R. Coleman, *Q-balls*, *Nucl. Phys. B* **262** (1985), no. 2 263. [Addendum: *Nucl.Phys.B* 269, 744 (1986)].
- [83] K.-M. Lee, J. A. Stein-Schabes, R. Watkins, and L. M. Widrow, *Gauged q Balls*, *Phys. Rev. D* **39** (1989) 1665.
- [84] I. E. Gulamov, E. Y. Nugaev, A. G. Panin, and M. N. Smolyakov, *Some properties of $U(1)$ gauged Q -balls*, *Phys. Rev. D* **92** (2015), no. 4 045011, [[arXiv:1506.05786](#)].
- [85] Y. Brihaye, A. Cisterna, B. Hartmann, and G. Luchini, *From topological to nontopological solitons: Kinks, domain walls, and Q -balls in a scalar field model with a nontrivial vacuum manifold*, *Phys. Rev. D* **92** (2015), no. 12 124061, [[arXiv:1511.02757](#)].
- [86] J. Heeck, A. Rajaraman, R. Riley, and C. B. Verhaaren, *Mapping Gauged Q -Balls*, *Phys. Rev. D* **103** (2021), no. 11 116004, [[arXiv:2103.06905](#)].
- [87] Y. Bai, S. Lu, and N. Orlofsky, *Q -monopole-ball: a topological and nontopological soliton*, *JHEP* **01** (2022) 109, [[arXiv:2111.10360](#)].
- [88] A. L. Macpherson and B. A. Campbell, *Biased discrete symmetry breaking and Fermi balls*, *Phys. Lett. B* **347** (1995) 205–210, [[hep-ph/9408387](#)].
- [89] L. Del Grosso, G. Franciolini, P. Pani, and A. Urbano, *Fermion soliton stars*, *Phys. Rev. D* **108** (2023), no. 4 044024, [[arXiv:2301.08709](#)].
- [90] M. B. Wise and Y. Zhang, *Stable Bound States of Asymmetric Dark Matter*, *Phys. Rev. D* **90** (2014), no. 5 055030, [[arXiv:1407.4121](#)]. [Erratum: *Phys.Rev.D* 91, 039907 (2015)].
- [91] M. B. Wise and Y. Zhang, *Yukawa Bound States of a Large Number of Fermions*, *JHEP* **02** (2015) 023, [[arXiv:1411.1772](#)]. [Erratum: *JHEP* 10, 165 (2015)].
- [92] E. Hardy, R. Lasenby, J. March-Russell, and S. M. West, *Big Bang Synthesis of Nuclear Dark Matter*, *JHEP* **06** (2015) 011, [[arXiv:1411.3739](#)].
- [93] M. I. Gresham, H. K. Lou, and K. M. Zurek, *Nuclear Structure of Bound States of Asymmetric Dark Matter*, *Phys. Rev. D* **96** (2017), no. 9 096012, [[arXiv:1707.02313](#)].
- [94] M. I. Gresham, H. K. Lou, and K. M. Zurek, *Early Universe synthesis of asymmetric dark matter nuggets*, *Phys. Rev. D* **97** (2018), no. 3 036003, [[arXiv:1707.02316](#)].
- [95] C. Kouvaris and N. G. Nielsen, *Asymmetric Dark Matter Stars*, *Phys. Rev. D* **92** (2015), no. 6 063526, [[arXiv:1507.00959](#)].

- [96] G. F. Giudice, M. McCullough, and A. Urbano, *Hunting for Dark Particles with Gravitational Waves*, *JCAP* **10** (2016) 001, [[arXiv:1605.01209](#)].
- [97] A. Maselli, P. Pnigouras, N. G. Nielsen, C. Kouvaris, and K. D. Kokkotas, *Dark stars: gravitational and electromagnetic observables*, *Phys. Rev. D* **96** (2017), no. 2 023005, [[arXiv:1704.07286](#)].
- [98] D. Curtin and J. Setford, *How To Discover Mirror Stars*, *Phys. Lett. B* **804** (2020) 135391, [[arXiv:1909.04071](#)].
- [99] D. Curtin and J. Setford, *Signatures of Mirror Stars*, *JHEP* **03** (2020) 041, [[arXiv:1909.04072](#)].
- [100] M. Hippert, J. Setford, H. Tan, D. Curtin, J. Noronha-Hostler, and N. Yunes, *Mirror neutron stars*, *Phys. Rev. D* **106** (2022), no. 3 035025, [[arXiv:2103.01965](#)].
- [101] C. Gross, G. Landini, A. Strumia, and D. Teresi, *Dark Matter as dark dwarfs and other macroscopic objects: multiverse relics?*, *JHEP* **09** (2021) 033, [[arXiv:2105.02840](#)].
- [102] M. Ryan and D. Radice, *Exotic compact objects: The dark white dwarf*, *Phys. Rev. D* **105** (2022), no. 11 115034, [[arXiv:2201.05626](#)].
- [103] Y. Bai, S. Lu, and N. Orlofsky, *Dark exoplanets*, *Phys. Rev. D* **108** (2023), no. 10 103026, [[arXiv:2303.12129](#)].
- [104] Y. Bai and N. Orlofsky, *Primordial Extremal Black Holes as Dark Matter*, *Phys. Rev. D* **101** (2020), no. 5 055006, [[arXiv:1906.04858](#)].
- [105] M. Enoki and M. Nagashima, *The Effect of Orbital Eccentricity on Gravitational Wave Background Radiation from Cosmological Binaries*, *Prog. Theor. Phys.* **117** (2007) 241, [[astro-ph/0609377](#)].
- [106] M. Maggiore, *Gravitational Waves: Volume 1: Theory and Experiments*. Oxford University Press, 10, 2007.
- [107] P. Ajith et al., *A Template bank for gravitational waveforms from coalescing binary black holes. I. Non-spinning binaries*, *Phys. Rev. D* **77** (2008) 104017, [[arXiv:0710.2335](#)]. [Erratum: *Phys.Rev.D* 79, 129901 (2009)].
- [108] X.-J. Zhu, E. Howell, T. Regimbau, D. Blair, and Z.-H. Zhu, *Stochastic Gravitational Wave Background from Coalescing Binary Black Holes*, *Astrophys. J.* **739** (2011) 86, [[arXiv:1104.3565](#)].
- [109] **Planck** Collaboration, N. Aghanim et al., *Planck 2018 results. VI. Cosmological parameters*, *Astron. Astrophys.* **641** (2020) A6, [[arXiv:1807.06209](#)]. [Erratum: *Astron.Astrophys.* 652, C4 (2021)].
- [110] C. J. Moore, R. H. Cole, and C. P. L. Berry, *Gravitational-wave sensitivity curves*, *Class. Quant. Grav.* **32** (2015), no. 1 015014, [[arXiv:1408.0740](#)].
- [111] K. Schmitz, *New Sensitivity Curves for Gravitational-Wave Signals from Cosmological Phase Transitions*, *JHEP* **01** (2021) 097, [[arXiv:2002.04615](#)].
- [112] **VIRGO** Collaboration, F. Acernese et al., *Advanced Virgo: a second-generation interferometric gravitational wave detector*, *Class. Quant. Grav.* **32** (2015), no. 2 024001, [[arXiv:1408.3978](#)].
- [113] W.-H. Ruan, C. Liu, Z.-K. Guo, Y.-L. Wu, and R.-G. Cai, *The LISA-Taiji network*,

- Nature Astron.* **4** (2020) 108–109, [[arXiv:2002.03603](#)].
- [114] K. Abazajian et al., *CMB-S4 Science Case, Reference Design, and Project Plan*, [arXiv:1907.04473](#).
 - [115] F.-Y. Li, M.-X. Tang, and D.-P. Shi, *Electromagnetic response of a Gaussian beam to high frequency relic gravitational waves in quintessential inflationary models*, *Phys. Rev. D* **67** (2003) 104008, [[gr-qc/0306092](#)].
 - [116] N. Aggarwal et al., *Challenges and opportunities of gravitational-wave searches at MHz to GHz frequencies*, *Living Rev. Rel.* **24** (2021), no. 1 4, [[arXiv:2011.12414](#)].
 - [117] A. Ringwald, J. Schütte-Engel, and C. Tamarit, *Gravitational Waves as a Big Bang Thermometer*, *JCAP* **03** (2021) 054, [[arXiv:2011.04731](#)].
 - [118] G. Franciolini, A. Maharana, and F. Muia, *Hunt for light primordial black hole dark matter with ultrahigh-frequency gravitational waves*, *Phys. Rev. D* **106** (2022), no. 10 103520, [[arXiv:2205.02153](#)].
 - [119] R. F. Dielectric, D. Schmitt, and L. Sagunski, *Binary Systems in Massive Scalar-Tensor Theories: Next-to-Leading Order Gravitational Waveform from Effective Field Theory*, [arXiv:2311.04274](#).
 - [120] L. Liu, Z.-K. Guo, R.-G. Cai, and S. P. Kim, *Merger rate distribution of primordial black hole binaries with electric charges*, *Phys. Rev. D* **102** (2020), no. 4 043508, [[arXiv:2001.02984](#)].
 - [121] P. C. Peters and J. Mathews, *Gravitational radiation from point masses in a Keplerian orbit*, *Phys. Rev.* **131** (1963) 435–439.